Thesis for the degree of doctor of philosophy

Differential Magnetic Biosensor using HTS SQUID Gradiometer

A step toward point-of-care diagnostics

Sobhan Sepehri

CHALMERS
UNIVERSITY OF TECHNOLOGY

Department of Microtechnology and Nanoscience - MC2
Quantum Device Physics Laboratory
Chalmers University of Technology
Göteborg, Sweden 2019

Differential Magnetic Biosensor using HTS SQUID Gradiometer
A step toward point-of-care diagnostics
SOBHAN SEPEHRI
ISBN 978-91-7905-208-9

Doktorsavhandlingar vid Chalmers tekniska högskola
Ny serie nr. 4675
ISSN 0346-718X

Quantum Device Physics Laboratory
Department of Microtechnology and Nanoscience- MC2
Chalmers University of Technology
SE-412 96 Göteborg, Sweden
Telephone +46 31 772 1000

Cover: Sketch of the configuration of two microfluidic channels above a 1st order planar gradiometer SQUID sensor. The differential measurement removes the unbound MNPs from the positive test sample.

Printed by Reproservice
Göteborg, Sweden 2019

Differential Magnetic Biosensor using HTS SQUID Gradiometer
A step toward point-of-care diagnostics
SOBHAN SEPEHRI
Department Microtechnology and Nanoscience
Chalmers University of Technology
Göteborg, Sweden 2019

Abstract

A fundamental tool for containing an epidemic outbreak and mitigating its effects is early diagnostics. Currently, most of the diagnostic tests are performed by trained staff in centralized labs, which are expensive and time-consuming to establish and operate. Lack of access to such facilities could have devastating effects. The principal motivation behind point-of-care diagnostic systems is to provide a low cost, fast, sensitive, and specific test in the field which does not require highly skilled staff to operate.

This thesis describes a magnetic biosensor which takes advantage of a high-T_c superconducting quantum interference device (SQUID) gradiometer sensor and magnetic nanoparticles (MNPs) to develop a diagnostic unit for point-of-care. Rolling circle amplification (RCA) is used as the primary molecular amplification method. RCA is an isothermal process with very high specificity. It is, therefore, easy to implement in a mix and measure concept of a homogeneous assay. The specific binding of the MNPs to the products of the RCA (i.e., DNA coils) changes their relaxation dynamics which is detected by sensitive ac magnetic susceptibility measurement.

One of the issues with homogeneous magnetic assays, which limits their sensitivity, is the presence of excess MNP labels in the test sample solution. To mitigate this problem, a novel technique is introduced, which takes advantage of the geometry of our gradiometer sensor for a differential ac magnetic susceptibility measurement. In this technique, a negative control sample and a positive test sample are measured in a single measurement. The differential measurement virtually removes all of the unbound MNPs in the test sample and is analogous to the physical washing step typically used in conventional assays. This technique also provides better signal to noise ratio (SNR) and can detect target concentrations down to tens of femtomolar levels (45 fM).

To eliminate the use of liquid nitrogen (LN_2) for cooling of the SQUID sensor (as it is not abundantly available in the field) we have shown the successful operation of a SQUID gradiometer sensor on a commercially available micro-cooler platform. The operation of the SQUID on the micro-cooler and the high sensitivity of the novel differential ac susceptibility technique, realized in this work, are critical steps towards a homogeneous magnetic nucleic acid biosensor for rapid detection of diseases. The methods and instruments that are adopted and presented here are generic and could, in principle, be used for other targets such as Influenza, Ebola, and Zika. With full implementation of the molecular amplification on a disposable lab-on-a-chip, the unit would be promising for rapid and highly sensitive diagnostics at the point-of-care.

Keywords: magnetic bioassay, biosensor, high-T_c SQUID, rolling circle amplification, RCA, magnetic nanoparticle, microfluidics, differential ac susceptibility, diagnostics, point-of-care.

ما را به سخت جانی خود این گمان نبود!

از گلشن شیخ

Acknowledgements

It is close to a decade I am trying to get a Ph.D. degree. Everyone back home has started to wonder "*What is this Ph.D. that never finishes?*". It was a long journey, and it had its ups and downs. From failing to secure funding or a position to a rejected visa and toxic work environment. What I did despite all of that misfortune was refusing to give up, and here I am, finishing this decade happily and soon graduating from Chalmers. To be honest, I never knew myself to be such a die-hard (that is what it says in the Persian text, if you wondered). I owe it to many of you who believed in me and supported me in this journey. I learned a lot, grew as a person, and enjoyed/hated it all the way, like everything else in life.

I should first thank my supervisor Alexei Kalaboukhov. It was a pleasure working with you and having your support. Your energy and enthusiasm were a big driving force for me. Dag Winkler, my examiner, I am honored to have you on my side. You have been more of a friend to go to instead of a boss, and I never hesitated to drop by your office. Christer Johansson, it was a privilege to have you as a co-supervisor. Your passion and enthusiasm for magnetism and life have been inspirational. I want to also extend this gratitude to my other co-supervisor, Justin F. Schneiderman, for his assistance and feedback. I am grateful for getting the chance to work with you in Chalmers.

This work would not have been possible without the collaborations with Christer Johansson, Jakob Blomgren, Maria Strømme, Aldo Jesorka, Kiryl Kustanovich, Jan Albert, Mats Nilsson, Ivan Hernandez-Neuta and Felix Neumann. Aldo Jesorka, thank you for letting me into your lab. You are a remarkably talented chemist. Teresa Zardán Gómez de la Torre made valuable contributions with her samples from Uppsala and taught me the ABCs of the biochemistry. It was always a pleasure discussing magnetic bioassays (and beyond) with you, and I hope I have made an acceptable Teresa #2 out of myself.

Lars Jönsson, you have exceptionally skillful craftsmanship, and I learned a lot from you. You are a real asset to the quantum device physics laboratory (QDP). Susannah Carlsson, Maria Tremblay, Debora

Perlheden, and Linda Bråvell, I appreciate all your support. You are indeed the ones actually running this place.

Silvia Ruffieux, Christoph Pfeiffer, Minshu Xie, Bushra Riaz, and Maxim Chukharkin Leonidovich thank you for being great colleagues and friends. SQUID SQUAD thank you for the good runs and your help in the SQUID lab, 3rd place seems to be the best we could pull off. Silvia, it was a pleasure being your colleague and friend. I hope it lasts long so I can finally come to your farm and we go for some occasional donkey riding excursions. Edoardo, Gunta, and Marco, I enjoyed sharing an office with you, and I can only hope you did so too. Edoardo, thanks for the laughs and breaks. Now that Domenico is not around anymore, you may finally be the strongest one in the QDP. Special thanks also to all past and present members of the QDP. You have created a fantastic stimulating environment. I have also been lucky to have a big community of Iranians around, you guys literally made Sweden another Iran. As a good old tradition in the low temperature physics, I should also thank Gustav[1] for all his sneaky companionship.

Thank you, Hanna, for all the love and for making Sweden feel like home. I am lucky to have you and look forward to eating more fish and shellfish with you. But only the good ones from the V/Bästkusten. I wish to finally thank my family, especially my parents, Hamid and Mina, for their love, support, and patience. Dad, you have taught me not to be afraid, take risks, and believe that I can do anything. Mom, your love and support have kept my heart warm even from thousands of kilometers away. You have always encouraged me to learn more. I am grateful to have you both in my life!

Sobhan Sepehri, Göteborg, October 2019

[1]Gustav is the neighbor's cat.

Abbreviations

ATP adenosine triphosphate.

BNF bionized nanoferrite.

BSA bovine serum albumin.

CAD computer aided design.

CMOS complementary metal oxide semiconductor.

CRP c-reactive protein.

DNA deoxyribonucleic acid.

dNTP nucleotide triphosphate.

EDTA ethylenediaminetetraacetic acid.

ELISA enzyme-linked immunosorbent assay.

FDA food and drug administration.

FLL flux locked loop.

GMR giant magnetoresistance.

HRF high relaxation frequency.

HTS high temperature superconductor.

LAMP loop mediated isothermal amplification.

LCR ligase chain reaction.

LN_2 liquid nitrogen.

LOD limit of detection.

LRF low relaxation frequency.

LTS low temperature superconductor.

MEMS micro electro mechanical systems.

MNP magnetic nanoparticle.

MSR magnetically shielded room.

NaCl sodium chloride.

NC negative control.

NMR nuclear magnetic resonance.

NTA nanoparticles tracking analysis.

PBS phosphate-buffered saline.

PCR polymerase chain reaction.

PDMS poly(dimethylsiloxane).

PEG poly(ethylene glycol).

PEO poly(ethylene oxide).

PET poly(ethylene terephthalate).

POC point-of-care.

PSA prostate-specific antigen.

PVC polyvinyl chloride.

RCA rolling circle amplification.

RCP rolling circle product.

RNA ribonucleic acid.

SNR signal to noise ratio.

SQUID superconducting quantum interference device.

TEM transmission electron microscopy.

Tris-HCl tris(hydroxymethyl) aminomethane hydrochloride.

Tween-20 polysorbate 20.

YBCO yttrium barium copper oxide $YBa_2Cu_3O_{7-\delta}$.

List of appended papers

This thesis is based on the work contained in the following papers:

I. A. Kalabukhov, E. J. De Hoon, K. Kuit, P. P. P. Lerou, M. Chukharkin, J. F. Schneiderman, **S. Sepehri**, A. Sanz-Velasco, A. Jesorka, and D. Winkler. "Operation of a high-T_c SQUID gradiometer with a two-stage MEMS-based Joule-Thomson micro-cooler".
Superconductor Science and Technology 29.9 (2016), p. 1–6.

II. **S. Sepehri**, E. Eriksson, A. Kalaboukhov, T. Zardán Gómez de la Torre, K. Kustanovich, A. Jesorka, J. F. Schneiderman, J. Blomgren, C. Johansson, M. Strømme, and D. Winkler. "Volume-amplified magnetic bioassay integrated with microfluidic sample handling and high- Tc SQUID magnetic readout".
APL Bioengineering 2.1 (2018), p. 016102.

III. **S. Sepehri**, T. Zardán Gómez de la Torre, J. F. Schneiderman, J. Blomgren, A. Jesorka, C. Johansson, M. Nilsson, J. Albert, M. Strømme, D. Winkler, and A. Kalaboukhov. "Homogeneous differential magnetic assay".
ACS Sensors 4 (2019), p. 2381-2388.

IV. **S. Sepehri**, B. Agnarsson, T. Zardán Gómez De La Torre, J. F. Schneiderman, J. Blomgren, A. Jesorka, C. Johansson, M. Nilsson, J. Albert, M. Strømme, D. Winkler, and A. Kalaboukhov. "Characterization of binding of magnetic nanoparticles to rolling circle amplification products by turn-on magnetic assay".
Biosensors 9 (2019), p. 109.

V. J. Blomgren, F. Ahrentorp, D. Ilver, C. Jonasson, **S. Sepehri**, A. Kalaboukhov, D. Winkler, T. Zardán Gómez De La Torre, M. Strømme, and C. Johansson. "Development of a Sensitive Induction-Based Magnetic Nanoparticle Biodetection Method".
Nanomaterials 8 (2018), p. 887.

Other papers and publications:

I. F. Ahrentorp, J. Blomgren, C. Jonasson, A. Sarwe, **S. Sepehri**, E. Eriksson, A. Kalaboukhov, A. Jesorka, D. Winkler, J. F. Schneiderman, M. Nilsson, J. Albert, T. Zardán Gómez de la Torre, M. Strømme, and C. Johansson. "Sensitive magnetic biodetection using magnetic multi-core nanoparticles and RCA coils".
Journal of Magnetism and Magnetic Materials 427 (2017), p. 14–18.

Contents

CHAPTER 1

Introduction

Pandemics can have grave consequences on global human health, economics, and well-being [1]. Influenza pandemics are unpredictable and recurring events with unclear associated global mortality. Influenza-related mortality is underestimated mostly due to absence of routine laboratory tests and difficulties in identifying influenza-related deaths. Models show at least an order of magnitude underestimation in the 2009 pandemic influenza A H1N1 confirmed death count [2]. The pandemic influenza in 1918 infected half of the world population and caused over 50 million deaths [3]. Today, the world is a different place, and with advances in science, technology, and medicine, we are not confined to the limits of the early 20^{th} century health care. The three later pandemics of influenza that occurred in 1957, 1968, and 2009 did not reach the same scale nor severity of the 1918 pandemic; however, the threat remains.

Diagnostic tests are now a part of everyday life. They are either used by the patient at home, like pregnancy tests or glucose monitors, or are performed in a clinical lab on patient's samples such as blood, urine, stool, etc. As an essential part of medical care, they are used for diagnosis or exclusion of a particular disease, monitoring the control of a disease, or screening diseases at pre-symptomatic stage. Early diag-

nosis is a fundamental component in containing an epidemic/pandemic outbreak [4]. Lack of access to laboratory diagnostics in low or middle-income countries is a great challenge which could result in late and/or incorrect diagnosis and ineffective treatment [5]. However, establishing a diagnostic laboratory in such environments is a complicated and expensive task and takes a rather long time during which an outbreak can become an epidemic. Therefore, the development of a fast, sensitive, and low cost point-of-care (POC) diagnostic system with high specificity is crucial for controlling the spread of infectious diseases. The implications of which is huge in reducing the suffering of the population and the costs of epidemics on the society, and saving lives.

1.1 Biosensors

Biosensors are powerful tools in the clinical analysis of viruses and various diseases, where a rapid and timely diagnosis is crucial for public health. Currently, most of these tests are performed in centralized laboratories using large automated clinical analyzers which are costly and require specialized staff and long analysis time [6]. To bring these test to the POC, a user-friendly instrument without the need for trained staff is required. Biosensors have great opportunity to be used at the POC. They are analytical devices and consist of a bio-recognition element and a sensor. These two components are well incorporated, and the interaction of the bio-recognition element with the target analyte is transduced into a signal which can be measured by the sensor. The bio-recognition element is responsible for the selectivity of the biosensor [7]. It is made from a biological or biologically derived materials such as tissues, microorganisms, enzymes, nucleic acids, antibodies, proteins, aptamers, etc. [8]. The interaction of the analyte with the bio-recognition element produces an optical, electrochemical, thermometric, piezoelectric, mass-based, magnetic, mechanical, or any other effect which the sensor converts into a signal. The most common bio-recognition interactions are antigen-antibody, enzymatic, cellular (e.g., within or between microorganisms), nucleic acid-based, and biomimetic based interactions [9].

Biosensors can qualitatively and/or quantitatively detect target analytes of both biological (e.g., antibodies, DNA/RNA molecules, pro-

teins, enzymes, etc.) [10] and non-biological nature (e.g., ions, dissolved gases, drugs, and toxins) [11]. The application of biosensors is not limited to the diagnosis of diseases. The diverseness, high sensitivity, and specificity of biosensors are also crucial for a wide variety of other applications including health, safety, and environmental assessments such as pharmaceutical analysis, drug monitoring, clinical pharmacokinetics, environmental monitoring, and pollutant detection [12].

Nucleic acid assays are a group of biosensors that adopt deoxyribonucleic acid (DNA) as the bioreceptor. They use a single-strand DNA which hybridizes to its complementary strand with good specificity to realize the detection of a specific DNA or ribonucleic acid (RNA) target. These nucleic acid assays can be used to detect pathogens, infection diseases, etc. Functionalized nucleic acids like aptamers and DNA enzymes have broadened the scope of applications for which they are used, to detect inorganic and organic molecules and even organisms [13]. Nucleic acid assays are simple and accurate due to the DNA hybridization technique and therefore, have attracted much attention leading to new developments and technologies. The sensitivity of these assays depends mainly on three factors: the efficiency of the DNA sequence hybridization, the sequence amplification method, and sensor sensitivity. The hybridization efficiency is affected by the structure of the probe and target DNA, the hybridization condition and molecular interactions [14]. The sequence amplification step could be used to reach higher sensitivities that are required in diagnostic laboratories. There are several amplification methods available, such as polymerase chain reaction (PCR) [15], loop mediated isothermal amplification (LAMP) [16], ligase chain reaction (LCR) [17], and rolling circle amplification (RCA) [18]. Many of the signal transduction methods mentioned earlier, e.g., fluorescence, electrochemistry, among others are currently used in nucleic acid assays. However, sensitive signal transduction is still one of the bottlenecks biosensors face in practical applications.

With advances in nanomaterials, nanotechnology is playing a significant and increasing role in the development of biosensors [19]. Nanomaterials such as gold nanoparticles [20], carbon nanotubes, magnetic nanoparticles [21], and quantum dots are now widely used in biosen-

sors [20]. The new nanotechnology-enabled biosensors provide solutions in physical, chemical, and biological sensing and have further improved the detection sensitivity, specificity, multiplexing capability, and portability of such systems. The application of nanotechnology in biosensors makes it possible to have biosensor arrays for high throughput parallel measurements, including the integration with microfluidics for lab-on-a-chip devices [10]. Although commercialization of biosensors lags the scientific research and patents, many of the hurdles towards POC tests have been overcome and the number of available POC biosensors for clinical applications has increased [22]. Magnetic nanoparticles (MNPs) have a wide range of applications in biology and medicine including biosensing [23, 24, 25]. Developments in the proper coatings of MNPs have given them biological recognition functions [26]. Bioassays based on MNPs have the advantage of real-time detection and low level of magnetic background signal from the biological samples. They do not require immobilization or intermediate washing steps, making them advantageous for biosensing [27]. Using MNPs in biosensing has contributed substantially to the field and its applications. Biosensors based on these nanomaterials have proven to have advantages in enhanced sensitivity, low limit of detection (LOD), high signal to noise ratio (SNR), and shorter analysis time compared with non-MNP-based strategies [28]. In sensing applications, MNPs are used in different ways including being integrated into the transducer materials, substrates for binding, labels, dispersion of the MNPs in the sample followed by their attraction onto the active detection surface of the biosensor [29, 30].

There are several magnetic detection techniques used in biosensors for detecting the MNPs and they can in general be categorized as either heterogeneous or homogeneous [21, 31]. The heterogeneous biosensors rely on diffusion of the analytes to the surface of a sensor and can be extremely sensitive, have a broad dynamic range, and have multiplexing capabilities [24]. For instance, a high-density giant magnetoresistance (GMR) sensor has been used to measure the kinetics of antigen-antibody binding at concentrations of 20 zeptomolar [32]. However, these biosensors are laborious and time-consuming as they require sample and substrate preparations, and multiple washing and incubating steps. Homogeneous biosensors, on the other hand, are simple to use with the signal

generated in the whole sample volume. Examples of such systems with high sensitivity are the nuclear magnetic resonance (NMR) system [33], ac magnetic susceptometry [34] and relaxometry using superconducting quantum interference device (SQUID) biosensors [35]. The homogeneous biosensors suffer from lower signal levels compared to the heterogeneous ones. The magnetic signal, in this case, comes from the whole volume of the sample and attenuates rapidly with distance from the source. Furthermore, the measurement of a weak detection signal is more challenging due to the presence of a high level of magnetic background from unbound magnetic markers.

1.2 Aim and scope

The aim of this work is the development of a sensitive magnetic nucleic acid assay for POC diagnostics. It uses MNP labels, a high-T_c SQUID gradiometer sensor and microfluidic sample handling. Padlock probe ligation [36] is exploited for target recognition followed by volume amplification using RCA [18]. The detection of the target nucleic acid is based on the immobilization of MNP labels on rolling circle products (RCPs) and is measured using ac magnetic susceptibility. The development is a part of the "FLU-ID" grant (No. SBE13-0125) supported by the Swedish Foundation for Strategic Research, SSF. The ultimate goal of the project is to develop a portable nano-diagnostics unit for detection of pandemic influenza. The unit should have low cost, fast response, and high specificity and sensitivity.

The thesis provides an overview and the background for the work presented in the appended papers. In Chapter 2, I briefly describe the relevant elements of magnetic biosensors, including the MNPs we use as labels, and the ac susceptibility detection approaches. Chapter 3 gives a short introduction into the principles of nucleic acid detection and presents the SQUID gradiometer sensors integrated with the microfluidic chip (i.e., the experimental setup). It also describes the novel differential ac susceptibility measurement technique we have developed. Chapter 4 includes the results and discussions for two different approaches used to quantify the target DNAs. Chapter 5 summarizes the performance of our biosensor and gives an outlook on future work towards a POC

nano-diagnostic unit.

CHAPTER 2

Magnetic nanoparticles and biosensing

2.1 Magnetic nanoparticles

MNPs are used in a broad field of applications including physics, chemistry, biology and medicine [23, 37, 38]. They are increasingly used in biosensors for their unique properties. They are biocompatible, have both physical and chemical stability [33], and high surface-to-volume ratio. MNPs are made from a variety of materials such as: iron-based: maghemite (γ-Fe_2O_3), magnetite (Fe_3O_4), $MgFe_2O_4$, FePt; cobalt-based: CoPt, Co; nickel-based: $NiFe_2O_4$, NiO; among many others [39]. Iron oxide MNPs are among the most commonly used magnetic materials and are prevalent compared to the other MNP materials due to their biocompatibility and minimal toxicity [40]. Magnetite and maghemite are both approved by the American food and drug administration (FDA) as magnetic materials for human *in vivo* applications [41].

The bio-functionalization of the MNPs with appropriate coating with biocompatible materials has lead to numerous biomedical applications of the MNPs. The interaction of the surface coating of the MNPs with

the biological media such as biological fluids, proteins, cell membranes, DNA, etc. may change certain properties of the particles' coating [39]. Therefore, the nature and quality of the coatings are important for the particles stability and their biomedical applications, especially for *in vivo* applications. A few examples of MNP coatings are polymers, proteins, peptides, oxides, etc. The MNPs we use in our experiments are commercial water/phosphate-buffered saline (PBS) suspended multi-core bionized nanoferrite (BNF) Fe_3O_4 particles of 100 nm in size from micromod Partikeltechnologie GmbH. They are prepared via a core-shell method which embeds the core magnetite in a non-magnetic shell of hydroxyethyl starch, which is a biopolymer material. The coating of these MNPs with streptavidin enables the bio-functionalization of the MNPs with different probing tags.

2.1.1 Magnetic moment of magnetic materials

One of the key parameters of any magnetic material, macroscopic or microscopic, is the magnetic moment which defines the magnetic strength of the object. The magnetic properties of the material are due to its intrinsic magnetic moment defined by the atomic structure and temperature. Magnetic materials are classified into diamagnetic, paramagnetic, ferromagnetic, antiferromagnetic, and ferrimagnetic, based on their response to an external magnetic field [42]. All materials exhibit diamagnetic properties. Diamagnetism is a weak repulsion of the magnetic field and is easily overtaken by any other magnetic behavior possessed by the material. Typical examples of diamagnetic materials are water, copper, and gold. Paramagnetism is due to uncoupled atomic magnetic moments in the material which in an external magnetic field aligned parallel to the direction of the field. The ferromagnetic materials also have uncoupled atomic magnetic moments but with a tendency to align in the same direction as one another, forming magnetic domains with a spontaneous magnetization even in the absence of an external field. The antiparallel arrangement of these uncoupled atomic magnetic moments in some materials would result in antiferromagnetism which leaves the materials with zero spontaneous magnetization. If the antiparallel arrangement of atomic magnetic moments in the material does not have equal magnitude, the material retains a spontaneous magnetization in

the absence of the external field and it is known to be ferrimagnetic. Some of the macroscopic behaviors of the ferrimagnets are similar to the ferromagnetic materials. Magnetite, maghemite are common ferrimagnetic materials and most iron, cobalt, and nickel alloys are ferromagnetic.

At the nanoscale, the magnetic properties of materials are different than in the bulk. The structure of the magnetic domains in the ferro/-ferrimagnetic materials determines the size dependency of its magnetic behavior. In bulk, the material has multiple domain structures separated by domain walls. Reducing the size of the magnetic material below a critical value, the energy which is necessary to divide into multiple domains becomes higher than the energy needed for the magnetic domain to be a single domain. This critical size corresponding to the single domain depends on the nature of the material and is in the range a hundred nanometers for magnetite [39]. Since the single domain particles are not exactly isotropic in their properties, the magnetic moment of the single domain points to a certain direction. In the absence of applied magnetic field and magnetic interaction between the particles, the total energy of a single domain particle with uniaxial anisotropy is:

$$E = KV_p sin^2\theta \tag{2.1}$$

where K is the magnetic anisotropy constant, V_p is the particles' magnetic core volume, and θ is the angle between the magnetic moment of the particle and easy axis [43, 44]. The KV_p is the energy barrier that separates the two equilibrium easy magnetization directions, given by the two directions of minimum energy (either $\theta = 0$ or $\theta = \pi$). The magnetization lies along either of the two directions of the minimum energy unless a perturbing force such as thermal agitation can switch the magnetization by taking it over the energy barrier. For small particles where this process occurs, the time average of the remanence is zero, and the particle exhibits properties of superparamagnetism [43]. It is though important to remember that this observation is intimately related to the timescale of the observation. In other words, an observed superparamagnetic behavior in one experimental timescale may be observed being in a so-called thermally blocked state in another experimental observation

with a shorter timescale. The superparamagnetism allows the colloidal stability of MNP suspension, particle manipulation, and collection upon exertion of an external magnetic field. Furthermore, in biomedical applications, where MNPs are used in a liquid suspension form, the random reorientation of the particles in the liquid suspension can also make a thermally blocked particle system exhibit superparamagnetic properties.

2.1.2 Magnetic relaxation processes

There are two mechanisms responsible for the relaxation of the magnetization of MNPs suspended in a liquid: Brownian relaxation where the MNPs change their magnetic orientation through a stochastic rotation of the particle itself and Néel relaxation where the magnetic moment of the particle changes its orientation within the particle overcoming the energy barrier due to anisotropy energy, Fig. 2.1. The relaxation associated with the former is described by Brownian relaxation time, τ_B, and is given by:

$$\tau_B = \frac{3\eta V_{hydro}}{k_B T} \tag{2.2}$$

where η is the viscosity of the carrier fluid, $V_{hydro} = \frac{3}{4}\pi r_H^3$ is the hydrodynamic volume of the particle including the core and its shell, k_B is the Boltzmann constant, and T is the temperature. The time decay associated with the latter is called the Néel relaxation time. Assuming a low applied magnetic field and no interaction between MNPs, the Néel relaxation time, τ_N, is given by:

$$\tau_N = \tau_0 \exp(\frac{KV_p}{k_B T}) \tag{2.3}$$

where τ_0 is a material-specific characteristic relaxation time typically in the range of $10^{-12} - 10^{-9}$ s [45]. KV_p is the energy barrier between different directions of easy magnetization where K is the magnetic anisotropy and V_p is the particle's magnetic core volume.

The Néel relaxation time changes the observed magnetic behavior of

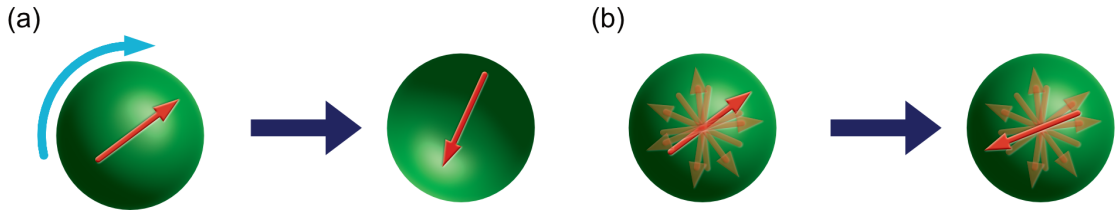

Figure 2.1: Illustration of magnetic nanoparticles relaxation mechanisms: (a) Brownian relaxation due to rotation of the suspended MNP in liquid and (b) Néel relaxation caused by reorientation of the magnetic moment inside the MNP.

the system with respect to the characteristic experimental measurement time τ_{exp}. If $\tau_{exp} \gg \tau_N$, the system reaches a thermodynamic equilibrium as the relaxation is faster than the magnetization orientation observed. The nanoparticles are then considered to be in a superparamagnetic state. However, for $\tau_{exp} \ll \tau_N$, the particle system is in the thermally blocked regime, and the magnetization will maintain its direction leading to a quasistatic state in the measurement time window. In this case, the particle magnetic moment is locked to itself and can magnetically be observed via the Brownian relaxation process.

The effective relaxation time of a liquid suspended MNP is a combination of the two characteristic times and is deduced using:

$$\frac{1}{\tau_{eff}} = \frac{1}{\tau_N} + \frac{1}{\tau_B}. \tag{2.4}$$

The effective relaxation time is dominated by the process with the shortest characteristic relaxation time. At a particular temperature (e.g., room temperature), the Néel relaxation is dominated by intrinsic properties of the MNP and the Brownian relaxation is dominated by external properties (i.e., viscosity) [46]. We use multi-core MNP of the particle's median size of 100 nm in our experiments. The multi-core MNPs contain several nanocrystals forming the core cluster which have the size of around 20 nm [47]. The magnetic properties of the particle depend on the properties of the nanocrystals and how they are distributed in the core (densely or loosely packed) [46]. The effective magnetic moment of the multi-core particles, thus, is the vector sum of all nanocrystals in the

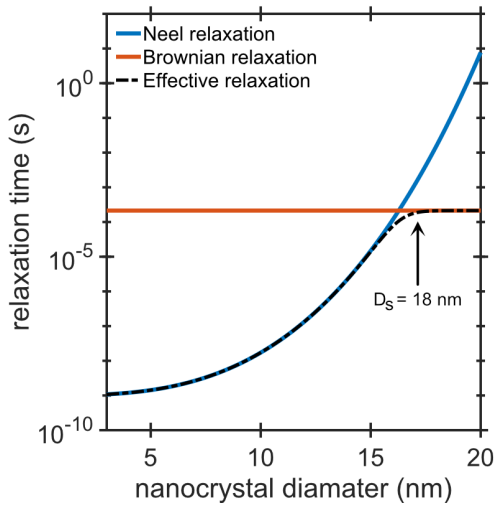

Figure 2.2: The Néel , Brownian, and effective relaxation times versus the diameter of the nanocrystals in the multi-core MNP with hydrodynamic particle size of 100 nm at a fixed temperature of 300 K with anisotropy constant of $K = 40kJ/m^3$, $\tau_0 = 10^{-9}$ and viscosity of $\eta = 10^{-3}Pa \cdot s$ [46]. The Brownian relaxation only depends on the hydrodynamic size of the MNP and is independent of the nanocrystal diameter. For the nanocrystal diameters smaller than $D_s = 18$ nm, the effective relaxation is dominated by the Néel relaxation. If the nanocrystals have diameters larger than D_S then the effective relaxation is dominated by the Brownian relaxation and the MNP will relax through rotation of the particle in the suspension liquid.

magnetic core [48]. Fig. 2.2 shows the Néel relaxation, Brownian relaxation and effective relaxation times for the multi-core 100 nm iron oxide MNP used in our experiments as a function of nanocrystals diameter in the core cluster. According to Eq. 2.2, the Brownian relaxation of the particle only depends on the particle's hydrodynamic size ($\approx$ 100 nm in this case) and is thus constant for all nanocrystal core diameter. If the nanocrystals in the MNP core matrix are smaller than $D_S = 18$ nm, the MNP relaxes through the Néel relaxation dynamic. For nanocrystal larger than D_S, on the other hand, the effective relaxation is dominated by Brownian relaxation. Immobilizing these MNPs by freezing drying results in total disappearance of the Brownian relaxation [46]. This indicates that the MNP system in the dispersion relaxes mostly through the Brownian relaxation process.

2.2 MNPs as labels for biosensing

Biosensing based on the MNPs is used as an analytical technique to detect variety of biomolecules e.g., DNA, antibody, proteins, etc. [10, 23]. Making use of different magnetic properties of the MNPs, the particles are used in variety of biosensors using different detection methods [24], for instance: measuring the the presence of the MNPs by permeability measurements [49], measuring changes in the hydrodynamic volume of the MNP [34], or by T_2 relaxation nuclear magnetic resonance which senses the particles surrounding environment [50]. There are also optical methods which use magnetic agitation to detect MNPs optically. Examples of such methods are: optomagnetic detection using Blu-ray laser [51], magneto-optical measuring of MNP relaxation time by Cotton-Mouton effect [52], etc. Another type of detection using MNPs relies on binding of the MNPs or the target molecules to the surface of the sensor such as sensors based on Hall effect [53, 54, 55], and giant magnetoresistance [32, 56, 57, 58], among others. These biosensors are called heterogeneous assays with a well-known example of heterogeneous immunoassays, the enzyme-linked immunosorbent assay (ELISA). Heterogeneous assays, in general, have wide dynamic range and high sensitivity. However, they are laborious, costly, and require multiple washing and incubating steps that make them unsuitable for POC diagnostics.

The detection method used in our biosensor is based on determining the change in the hydrodynamic size of the MNPs by measuring the change in Brownian relaxation dynamics. There are several methods to determine the variations in the hydrodynamic size of the MNPs. The first approach is called magnetorelaxometry [59, 60, 61, 62]. In this method, an external dc magnetic field is applied to align the MNPs and the time decay of the sample's magnetization is monitored after switching off the external magnetic field. After applying the pulsed-field, the time decay of magnetization for a MNP system with an effective relaxation time dominated by Brownian relaxation, is related to the random reorientation of particles which depends on the hydrodynamic volume of the particle. It is important to note that this observation is closely related to the measurement's timescale. The MNP system could appear to be superparamagnetic if the timescale of the measurement is

too long for measuring the remnant magnetization from MNPs in the quasistatic thermally blocked state. The time decay, on the other hand, is related to any alteration in the hydrodynamic size of the MNP, due to binding to target analytes.

The second method is to apply a rotating magnetic field to agitate the MNP sample [63]. The phase lag between the magnetization of the samples and the applied rotating magnetic field represents the hydrodynamic properties of the MNP system [64, 65]. The third approach, which we have used in our biosensor, is to apply an external ac magnetic field to actuate the MNPs. For small amplitudes, the magnetization of the MNP system is a linear function of the external magnetic field and is characterized by ac magnetic susceptibility. This approach is proposed theoretically by Connolly and St Pierre [66] and is shown for the first time experimentally for prostate-specific antigen [34]. The binding of the MNPs to the target analytes changes their hydrodynamic size and according to Eq. (2.2), their Brownian relaxation time. This specific binding and the induced change in the relaxation dynamic is detectable through measuring the ac magnetic susceptibility. The ac susceptibility has very low background signal (as the signal comes only from the MNP response to the excitation field) and is the center of our detection method. In the following sections, we explain this method in details.

2.2.1 Ac magnetic susceptibility

The Debye theory describes the frequency dependence of complex susceptibility of dispersive materials, such as polar molecules and ferrofluids [67]. This theory holds at low applied magnetic field amplitudes and for spherical particles when the magnetic dipole-dipole interaction is negligible compared to the thermal fluctuations. According to the Debye model, the magnetization of a collection of mono-dispersed, non-interaction particles is given by the complex susceptibility [68]:

$$\mathbf{M}(\omega) = \chi(\omega)\mathbf{H}_{ac}, \tag{2.5}$$

where $\mathbf{M}(\omega)$ is the complex magnetization, $\mathbf{H}_{ac}$ is the applied ac magnetic field, ω is the angular frequency of the applied field ($\omega = 2\pi f$) and

$\chi(\omega)$ is the ac magnetic susceptibility [69]:

$$\begin{aligned} \chi(\omega) &= \chi'(\omega) - i\chi''(\omega), \\ \chi(\omega) &= \frac{\chi_0 - \chi_\infty}{1 + i\omega\tau} + \chi_\infty. \end{aligned} \tag{2.6}$$

The real (in-phase) and imaginary (out-of-phase) parts of the ac susceptibility are given by:

$$\chi' = \frac{\chi_0 - \chi_\infty}{1 + (\omega\tau)^2} + \chi_\infty, \tag{2.7}$$

$$\chi'' = \frac{(\chi_0 - \chi_\infty)\omega\tau}{1 + (\omega\tau)^2}. \tag{2.8}$$

where χ_0 is the static magnetic susceptibility (which depends on the particle effective magnetic moment [48]), χ_∞ is the high frequency susceptibility, and τ is the characteristic relaxation time. Although the expressions are borrowed from the Debye theory for the dielectric relaxation, one can derive these equations within the framework of the linear response theory [70]. In a regime where the frequency of the applied ac magnetic field is comparable to the magnetic relaxation of the system, the system may show some phase lag (dissipation). The relaxation time of the system can be extracted at $\omega\tau = 1$ where the imaginary part has a maximum.

Assuming that the relaxation process is dominated by the Brownian relaxation, we can assign $\tau = \tau_B$. Fig. 2.3 illustrate the ac magnetic susceptibility for three individual particle systems with different particle sizes that have the Brownian relaxation as the characteristic relaxation process. According to Eq. (2.2), the Brownian characteristic time of these particles depends on their hydrodynamic volume. Therefore, the particle system with greater size (volume) has a longer relaxation time.

In practice, the colloidal magnetic particles have a particle size distribution. One commonly used model for the size distribution of the magnetic particles is the log-normal distribution:

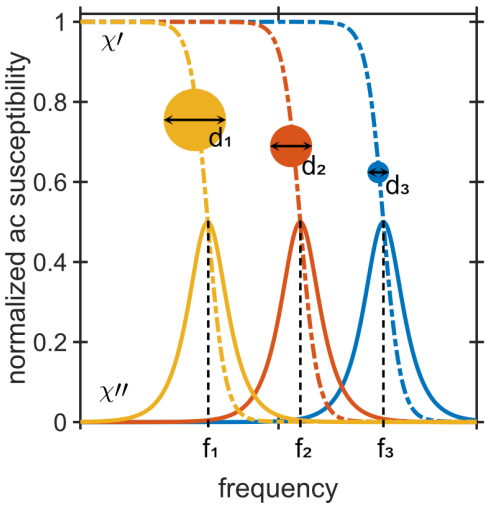

Figure 2.3: Normalized ac magnetic susceptibility for samples with 3 different particle sizes. The imaginary part of the susceptibility maximizes as the frequency approaches the Brownian relaxation frequency for each particle, $\omega\tau = 1$. Increasing the hydrodynamic diameter of the particles ($d_1 > d_2 > d_3$) shifts the relaxation dynamics to lower frequencies ($f_1 < f_2 < f_3$) and vice versa.

$$f(r_H) = \frac{1}{\sqrt{2\pi} r_H \ln \sigma} \exp[-\frac{(\ln r_H - \ln \bar{r_H})^2}{2 \ln^2 \sigma}] \tag{2.9}$$

where $\bar{r_H}$ is the median hydrodynamic radius and σ is the standard deviation, which defines the width of the distribution [59, 71]. Taking the size distribution of the MNP into account, the ac susceptibility then becomes:

$$\chi(\omega) = \int \frac{\chi_0}{1 + i\omega(r_H)} f(r_H) dr_H \tag{2.10}$$

where the $f(r_H)dr_H$ is the number of particles with radius between r_H and $r_H + dr_H$ [46]. By experimentally measuring the ac magnetic susceptibility $\chi(\omega)$, it is thus possible to estimate the relaxation time and the particle size distributions [72, 73].

2.2.2 Cole-Cole model

Dispersion of frequency-dependent ac susceptibility from the MNPs with distribution in relaxation time obeys the following phenomenological for-

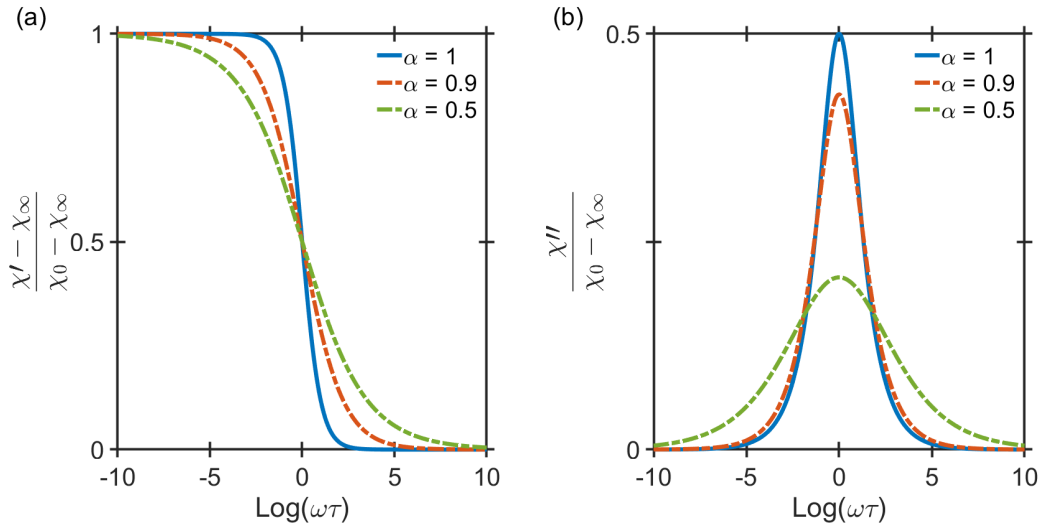

Figure 2.4: Examples of the real (a) and imaginary (b) parts of ac magnetic susceptibility for the Cole-Cole model Eq. (2.11). For $\alpha = 1$, the solid blue curves, the Cole-Cole model reduces to the Debye model Eq. (2.5). The red and green dashed lines represent the Cole-Cole model with different phenomenological parameters of $\alpha = 0.9$ and $\alpha = 0.5$, respectively.

mula:

$$\chi(\omega) = \chi_\infty + \frac{\chi_0 - \chi_\infty}{1 + (i\omega\tau)^\alpha} \tag{2.11}$$

where τ is the relaxation time, χ_∞ is the high-frequency susceptibility, and α is the phenomenological parameter which defines the span of the relaxation time and can assume values between 0 and 1. This equation was developed by two brothers Kenneth and Robert Cole in 1941 [74]. The Cole-Cole model is also called the generalized Debye model and can be regarded as a superposition of multiple Debye models with the central relaxation time given by the inverse of the frequency of the peak position on the imaginary part of the susceptibility. It is based on the assumption that there is a distribution of relaxation times governing the system dynamics [70]. This equation reduces to the Debye formula, Eq. (2.5), for $\alpha = 1$. For $0 < \alpha < 1$, the maximum value of the peak χ'' decreases, and the dispersion broadens. Therefore, the α parameter represents the broadness of the relaxation time distribution, Fig. 2.4. This broadening of distribution does not affect the frequency at which the imaginary part maximizes but decreases its amplitude.

2.2.3 Multimodal Cole-Cole model

If we have a MNP system that is composed of two or more MNP entities with relaxation times of τ_1, τ_2, ... the total magnetization of the system is a sum of the magnetizations from each entity. The total susceptibility of the system is therefore, a sum of the susceptibility of each MNP entity comprising the system and we have:

$$\chi = \chi_1 + \chi_2 + \cdots + \chi_\infty \tag{2.12}$$

where χ_1, χ_2, ... are the susceptibilities of MNPs with relaxation times τ_1, τ_2, ..., and the χ_∞ is the high frequency susceptibility of the total system. Using a Cole-Cole model to describe each magnetic entity in the system, the total susceptibility of the MNP system can be generalized to a superposition model expressed as:

$$\chi(\omega) = \frac{\chi_1}{1 + (i\omega\tau_1)^{\alpha_1}} + \frac{\chi_2}{1 + (i\omega\tau_2)^{\alpha_2}} + \cdots + \chi_\infty \tag{2.13}$$

where τ_1, τ_2, ... are the relaxation time, and α_1, α_2, ... are the phenomenological width parameters for the 1^{st}, 2^{nd}, ... modes. The χ_∞ is the total high-frequency contribution in the real component of ac susceptibility of the MNP ensemble. Fig. 2.5 shows the imaginary component of ac magnetic susceptibility for a MNP system which consists of MNPs with two size distributions with the median sizes of 100 and 300 nm, described by Eq. (2.13). The multimodal Cole-Cole model is fitted to the imaginary part of the ac susceptibility to extract the relaxation times and model the ac susceptibility response. When the two relaxation times of the two MNP entities (here in Fig. 2.5 MNPs of 100 and 300 nm) are well separated, two distinct relaxation times can be observed. Otherwise, the two peaks will merge into an asymmetric response curve with a single peak value.

2.2.4 Biosensing approaches with ac magnetic susceptibility

Several different approaches have been introduced based on ac susceptibility for biodetection [24]. The first approach is based on the shift

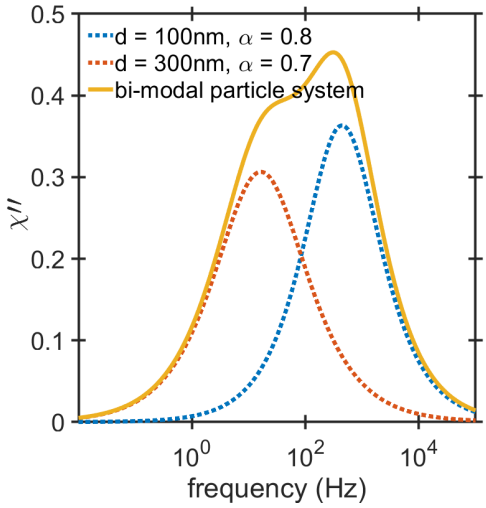

Figure 2.5: Imaginary part of ac magnetic susceptibility versus frequency for a two-MNP system comprising a mixture of a 100 nm and a 300 nm in size MNPs. The Cole-Cole model, Eq. (2.11), for individual particle systems, blue and red dashed curves, and the multimodal Cole-Cole model, Eq. (2.13), that models the bi-modal particle system, solid yellow curve, are plotted.

in relaxation frequency of the MNP labels due to binding interaction of the MNPs with target biomolecules. The frequency of the peak amplitude in the imaginary component of the ac magnetic susceptibility, which corresponds to the MNP labels, shifts to lower frequencies when the the hydrodynamic volumes of the MNP labels increase due to binding to the targets. Fig. 2.6 (a) illustrates the concept of the detection approach and the shift in the frequency of the imaginary part of the ac magnetic susceptibility. The application of this method for detecting biomolecules have been verified by detecting: prostate-specific antigen (PSA) in a solution using MNP labeled with PSA specific antibodies [34, 62] with typical LOD of 0.7 nM [62], biotinylated **S**-protein with avidin coated MNP labels [75, 76] with experimental measurement of 6.3µM **S**-protein [75], Brucella antibodies in serum samples from infected cows using lipopolysaccarides functionalized MNPs with detection limit of 0.05 µg/mL [77], target DNA molecules by hybridizing MNP labels functionalized with target complementary oligonucleotides with the DNA target with experimental limit of 33 pM [78]. This detection method, however, is not very sensitive due to broad particle size distribution and the shift in the ac susceptibility responses only occurs at high concentration of targets.

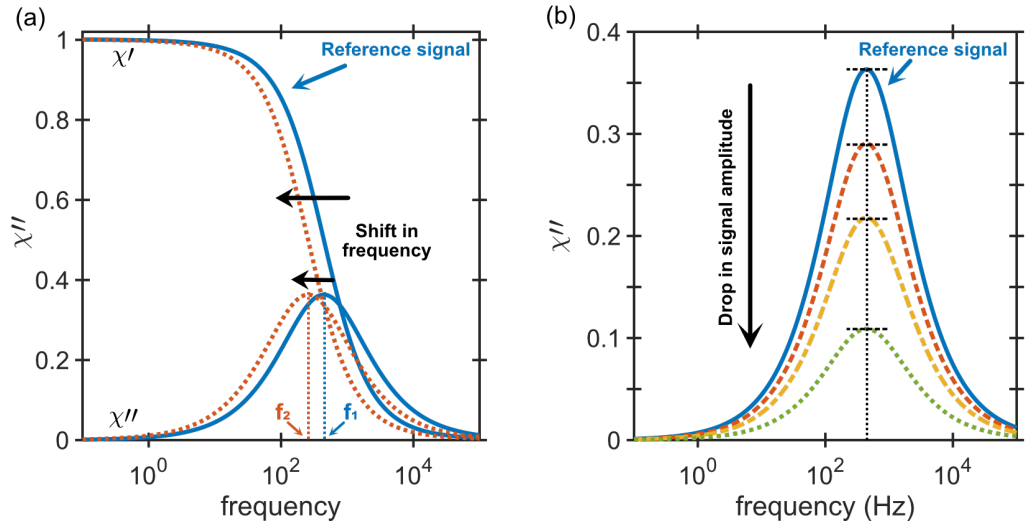

Figure 2.6: Frequency shift and turn-off biodetection using ac magnetic susceptibility measurement technique. (a) The detection signal is based on the shift in the imaginary component of ac susceptibility due to binding reaction with target molecule. The hydrodynamic size of the MNP labels increase upon binding with the target molecule and shifts the frequency of the imaginary ac susceptibility response to lower frequencies. (b) In the magnetic susceptibility reduction method, or turn-off detection approach, the amplitude of the ac magnetic susceptibility signal decreases upon binding of the target analytes with MNP labels.

Another approach to detect biomolecules focuses on the reduction in peak amplitude of the ac magnetic susceptibility of the MNP labels. The target-label complex either has a much larger hydrodynamic size or clusters, and therefore has its relaxation frequency well separated from the unbound MNP labels. This causes the amplitude of the imaginary part of the ac magnetic susceptibility at the relaxation frequency of the free MNP labels to reduce. Fig. 2.6 (b) shows an illustration of the magnetic susceptibility reduction method which is also known as the turn-off approach [79]. Target DNA molecules are detected using MNP labels functionalized with target complementary oligonucleotides using low-T_c SQUID with LOD of 3.7 pM [78], portable ac susceptometer with LOD of 4 pM [80], and high-T_c SQUID with LOD of 1 pM as we have reported in paper II. A mixed-frequency ac magnetic susceptibility reduction (with two ac excitation fields at two different frequencies) was used to measure avidin molecules using biotin coated MNP labels [81] and c-reactive protein (CRP) with MNP labels functionalized with anti-CRPs [82, 83]. Nonlinear magnetization of MNP with magnetic excitation at a combinatorial frequencies was also used in a magnetic immunoassay to detect *Yersinia pestis* and *Francisella tularensis* antigens, and *Legionella pneu-*

mophila bacteria [84]. Although this approach of detection has higher sensitivity to the target analyte compared to the earlier one, for low concentration of the target analyte the signal reduction is low and difficult to detect. The quantification of the target analyte in this case is sensitive to the disparities in the initial number of MNPs and the variations in signal when no target is present.

An alternative way of using the ac susceptibility is to use the phase representation of the ac magnetic susceptibility. According to Eq. 2.6, the susceptibility can be written in terms of phase and amplitude:

$$\chi(\omega) = \chi'(\omega) - i\chi''(\omega) = |\chi|e^{-i\theta}. \tag{2.14}$$

In this expression, θ is a measure of the phase angle between the external excitation field and the magnetization of the sample. It can be defined as an inverse tangent of the real and imaginary ac susceptibility as the following [65]:

$$\theta = arctan(\frac{\chi''}{\chi'}). \tag{2.15}$$

where χ' and χ'' are real and imaginary components of ac magnetic susceptibility. CRPs in human samples are detected using this method by forming magnetic clusters of functionalized iron oxide MNPs and CRPs [85]. The same principle has also successfully been applied (at frequencies below 10 Hz) in the optomagnetic measurement method [51] for detection of DNA targets [86]. In both of these two biosensors, the detection signal, which is the phase angle increases with increasing the concentration of target molecules. This method is called the turn-on detection strategy and is not limited to phase-based detection. Turn-on detection approach is also used in the imaginary part of ac magnetic susceptibility measurements to detect DNA targets using 40 nm MNP labels [87].

CHAPTER 3

Experimental methods

Biosensors are analytical devices utilizing the high sensitivity and selectivity of biological sensing. They are comprised of two main components: (I) a bioreceptor and (II) signal transduction. There is a diverse variety of biosensors combining different biological recognition elements with different signal transduction methods. In this chapter, we describe these two main components of our biosensor. First, we describe the basic principles and different steps of the nucleic acid assay used to detect the target DNA molecules. Nucleic acid assays are a group of biosensors that adopt DNA as bioreceptor. They use a single-strand DNA which hybridizes to its complementary strand with good specificity to realize the detection of a specific DNA or RNA target. These nucleic acid-based sensors can be used to detect not only pathogens, infection diseases but also inorganic and organic molecules and even organisms [13]. Here we use rolling circle amplification (RCA) to linearly amplify the recognized target DNA molecule, producing a rolling circle product (RCP) which has a larger hydrodynamic volume. The RCPs are results of the biodetection, and by labeling them with magnetic or fluorescent tags, we transduce the biorecognition into an optical (fluorescence) or a magnetic signal. The fluorescent-labeled RCPs are detected using nanoparticles tracking analysis (NTA) technique, basic principles of which is explained here. The

magnetically labelled RCPs are detected using a high-T_c SQUID gradiometer which is our main development. Sec. 3.3 describes the different components of the magnetic sensor in details which is then followed by calibration of the system using MNPs.

3.1 Nucleic acid assay

The genetic information encoded as a sequence of monomers in nucleic acids, DNA and RNA, are responsible for cellular function and consequently essential for all forms of life. The monomer building blocks are nucleotides which are made of a 5-carbon sugar, a phosphate group and a nitrogenous base. Nucleic acid diagnostics measure DNA or RNA in order to assay a particular nucleic acid sequence. To detect low abundant nucleic acids, numerous methods have been developed which selectively copy a specific and pre-defined nucleic acid sequence [88, 89].

The first and most commonly used nucleic acid amplification method is the PCR which has been broadly validated. The PCR technique relies on thermal cycling of the reaction for replication and amplifies a specific target DNA sequence to a large number of copies. Despite all its advantages, PCR has its limitations, such as high chances of false positives and contamination, sensitivity to specific contaminants, inhibitors, and thermal cycling [90].

There are several alternative amplification methods to PCR that offer potential advantages for speed, scale, cost and simplicity, e.g. LAMP [16], LCR [17], and RCA [18]. In our bioassay, we are using the RCA technique for amplification. RCA is an isothermal process and enables enzymatic amplification of the probe-target complex. The biomolecular detection technique utilizes a highly specific hybridization reaction between a probe molecule and a matching target forming a circular probe-target complex. This proves to be advantageous for genotyping or mutation detection in an unrelated background. The probe-target complex can then be amplified in order to achieve high sensitivity in a single-molecule detection [36, 90].

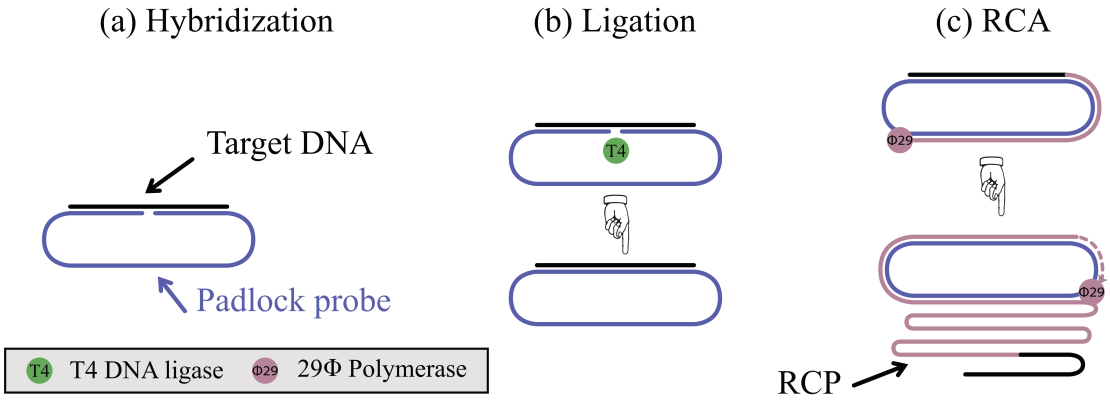

Figure 3.1: Illustration of (a) padlock probe recognition of target DNA, (b) ligation, (c) the amplification of the probes by RCA.

3.1.1 Target DNA recognition and enzymatic amplification

Engineered probing molecules are used for target recognition. These DNA molecules (padlock probes) are synthetic linear oligonucleotides, typically consisting of 70-100 nucleotides in length [91]. Around 20 outermost nucleotides at both $3'$ and $5'$ ends of the padlock probes are sequences complementary to the target DNA sequence. Therefore, they hybridize to the target DNA sequence in juxtaposition. The rest of the sequence linking the two hybridization arms are used for detection and identification. After the probes are hybridized to the targets, a ligase mediated process closes the nick in between the two ends and topologically locks the padlock to the target. The ligation process is susceptible to any mismatches at the $3'$ end of the padlock probe molecule. This allows an excellent sequence probing and detects any mutations down to single nucleotide [92, 93].

The circularized padlocks are then amplified by the continuous progression of Φ29 polymerase around the padlock probe replicating its complementary sequences. This process produces complimentary copies of the circularized probe-target complex, joining them end-to-end within a single DNA macromolecule [93]. This DNA molecule is also called DNA coils, or rolling circle products (RCPs). Fig. 3.1 is a cartoon that illustrates the different steps of the assay.

The amplification time determines the length of the RCP and one hour

reaction time produces around 1000 complementary copies. However, the amplification process is random and the final RCPs have a broad size distribution [94]. RCA is a linear process and each RCP corresponds to one single target DNA molecule. In a recent study by Kühnemund et al., the final concentration of the RCPs after the amplification is determined experimentally. This study shows that the actual number of the products is only 22.6% of the initial target DNA molecules [95]. The discrepancy is related to the imprecise determination of the concentration by the vendors, inefficiencies during ligation and amplification reactions. The protocols used for the ligation and amplification processes can be found in the Appendix A.

3.1.2 Fluorescent and magnetic labeling of RCPs

The RCPs can be analyzed by various methods including gel electrophoresis [96, 97], incorporation of fluorophore-conjugated nucleotide triphosphate (dNTP) for fluorescent microscopy and spectroscopy [98] or hybridization of complementary strands with fluorescence markers, gold nanoparticles [99], magnetic nanoparticle (MNP) [78], quantum dots [100], etc. In this work, we detected the RCPs optically and magnetically by addition of fluorescent or magnetic labels, respectively. The fluorescent or magnetic labels have oligonucleotides which are complementary to the linking part of the padlock probes. This allows them to bind to the RCPs by base-pair hybridization. The labels, therefore, crowd around the RCPs which then can be detected optically or magnetically.

In this work, both fluorescent-tagged detection oligonucleotides and functionalized streptavidin-coated MNPs are used as physical labels for optical and magnetic detection, respectively. The detection oligonucleotides have a biotin molecule on the $3'$ side and either Atto-488 or 6-Fam fluorescent dye on the $5'$ site. The detection oligonucleotides can be used as they are as fluorescent labels, however, the MNPs should be functionalized with the detection oligonucleotides before hybridization with the RCPs. The streptavidin coating of the MNPs has high affinity for the biotin molecule conjugated to the detection oligonucleotide. Therefore, the coupling of oligonucleotides to the MNPs surface makes them functional for specific binding to the RCPs. Fig. 3.2 illustrate the

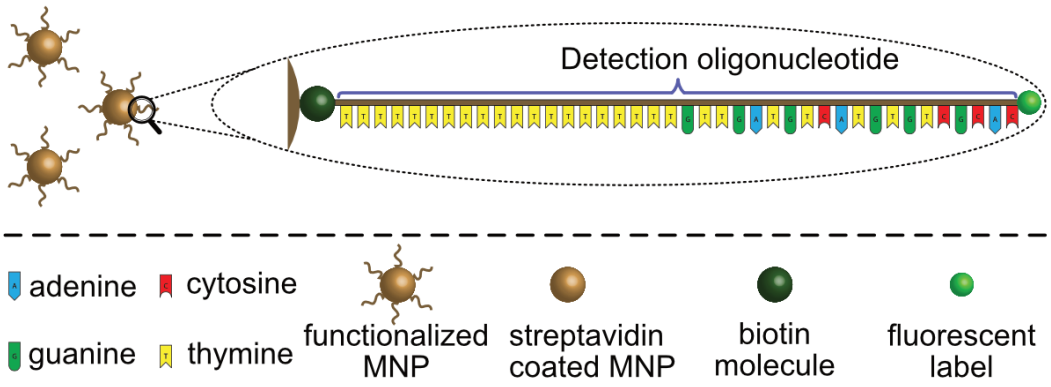

Figure 3.2: The detection oligonucleotide for labelling of RCPs from *Vibrio Cholerae* DNA target. The oligonucleotide has a biotin molecule on one side for coupling to MNPs and a fluorescent dye on the other side for optical detection. The oligonucleotide tags are bound to the streptavidin shell of the MNPs by high affinity and rapid biotin-streptavidin interaction.

different parts of a detection oligonucleotide. The conjugation of the optical and magnetic labels to the RCPs is performed by adding the labels to the RCP sample solution and incubating it at 55 °C for 20 min. During the hybridization the sample volume is kept small in order to increase the chance of the tags and the RCPs to meet.

3.2 Nanoparticle tracking analysis (NTA)

To detect the fluorescent-tagged RCPs, NTA is used. NTA utilizes a laser beam to detect the light scattering or fluorescence signal from the Brownian motion of the particles in liquid suspension in order to determine the particle size distribution. A laser beam of specific wavelength is passed into the sample chamber containing the nanoparticle suspension with reduced profile [101]. The particles in the path of the beam then scatter or absorb the light which is easily visible using a low magnification microscope objective, Fig. 3.3. A complementary metal oxide semiconductor (CMOS) camera records the particles movement in the fields of view. A software then identifies each particle and tracks its movements under Brownian motion on a frame by frame basis and calculates the average distances moved by individual particles. The spherical equivalent of the particle diameter, d, is given by the Stokes-Einstein equation:

$$D = kT/3\pi\eta d \tag{3.1}$$

where D is the particle's diffusion coefficient, k is the Boltzmann constant and T is the temperature. We use NanoSight LM20 (Nanosight, Amesbury, United Kingdom) which utilizes a 488-nm laser for NTA measurements. The samples are injected in the sample chamber using a sterile syringe and a syringe pump. The NTA 2.0 software is then used for capturing and analyzing the data.

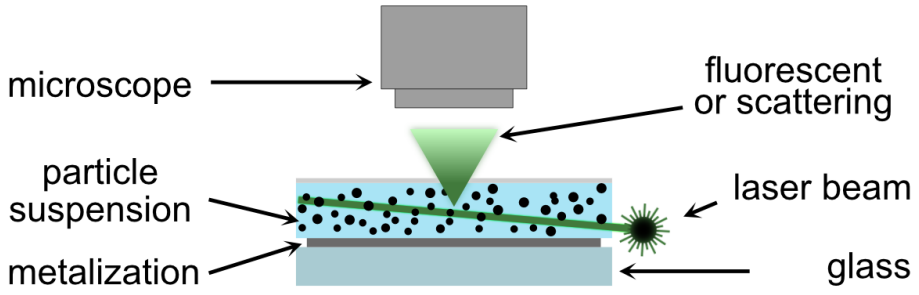

Figure 3.3: Schematic illustration of NTA system. A laser beam is passed into the particle suspension and the scatter or fluorescent light is collected using a microscope where the particles movements are recorded by a CMOS camera.

3.3 Ac magnetic susceptibility measurement setup

Magnetic ac susceptometry is a frequency domain measurement technique and provides information regarding the relaxation time and size distribution of the MNPs, see Sec. 2.2.1. The specific binding of the MNPs to the RCPs changes their hydrodynamic size. According to Eq. (2.2), this change in the hydrodynamic size affects the Brownian relaxation time of the MNPs. We have developed a biosensor for measurement of the MNPs (magnetic markers) in our bioassay using the ac magnetic susceptibility technique. The setup consists of:

- a high-T_c SQUID sensor,
- a liquid nitrogen (LN_2) cryostat or a micro-cooler to maintained SQUID sensor below its transition temperature,
- magnetic shielding or a magnetically shielded room (MSR),

- SQUID electronics to operate the sensor,
- microfluidic chips to bring the sample solutions to the detection areas above the SQUID sensor,
- a 3D-printed alignment frame mounted on the cryostat for controlling the position of the microfluidic chip above the sensor,
- a Helmholtz coil to apply homogeneous external ac magnetic field.

The measurement technique involves magnetization of MNPs by an external ac magnetic field produced by the Helmholtz coil and measuring the sample dynamic magnetic moment by the SQUID gradiometer. The in-phase and out-of-phase components of the SQUID signal acquired from magnetic samples are expressed as a voltage (or flux) read out from the SQUID electronics. The voltage is directly proportional to the magnetic moment of the sample. Since the magnetic susceptibility is only a calibration factor that converts the voltage to a sample magnetic moment (and ac susceptibility by dividing magnetic moment with field amplitude and sample volume), the voltage values are used as the sample's measured ac magnetic susceptibility. The calibration factor can be extracted by measuring a material with known magnetic characteristics like dysprosium oxide (Dy_2O_3) or by comparing the SQUID signal with another already calibrated instrument (like DynoMag, RISE Acreo) measuring the same sample.

A waveform generator (Fluke AWG-220) produces a sinusoidal wave which is amplified using a current amplifier to drive the Helmholtz coil. The coil can create a sinusoidal and homogeneous excitation field up to 350 µT, which is limited by the current amplifier. The excitation field is in the range of 0.5 Hz to 10 kHz. The SQUID signal is read out by Magnicon SEL-1 electronics. A Stanford SR-860 lock-in amplifier is used to extract the in-phase and out-of-phase components of the SQUID gradiometer signal having the current in the Helmholtz coil as a reference. The in-phase and out-of-phase signals are functions of real and imaginary components of the magnetic susceptibility from the magnetic samples, respectively. Fig. 3.4 shows a schematic diagram of the ac susceptibility measurement setup. To eliminate the residual coupling

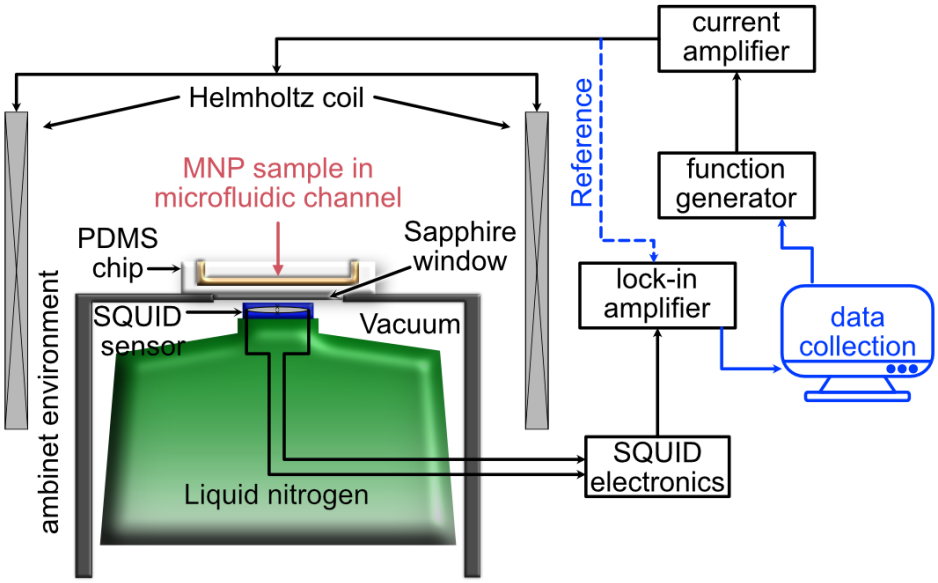

Figure 3.4: A schematic diagram of the lock-in measurement setup and a cross-section schematic illustration of the LN_2 cryostat for magnetic ac susceptibility measurements. The function generator through a current amplifier drives the Helmholtz coil to produce homogeneous ac magnetic excitation field. The SQUID readout signal from the SQUID electronics and a reference signal at excitation frequency, which is a voltage drop across a small resistor (0.01Ω) placed in line with the Helmholtz coil, are given to the lock-in amplifier for phase sensitive measurement. The in-phase and out-of-phase components of the signal are collected by a computer using a program interface in MATLAB ver. R2018b (The MathWorks, Inc., Natick, Massachusetts, United States).

of the excitation field to the pick-up coils, a calibration measurement is made without having any samples. This calibration is taken as the background signal, which is subtracted from all measurements. In the following sections, the details of different components of the ac magnetic susceptibility measurement setup are described.

3.3.1 High-T_c SQUID gradiometer sensor

To reach a very high sensitivity to the magnetically labeled RCPs, we need to have a sensitive magnetic sensor. The SQUID is a magnetic flux-to-voltage transducer and is among the most sensitive magnetic field sensors. It is made of a superconducting loop which contains one or two Josephson junctions. Josephson junctions are active devices in superconducting electronics and consists of two weakly coupled superconducting electrodes [102]. SQUIDs can be made using both low temperature superconductor (LTS) and high temperature superconductor (HTS) ma-

terials. The discovery of superconductivity in the yttrium barium copper oxide $YBa_2Cu_3O_{7-\delta}$ (YBCO) compound material with $T_C = 93\ K$ opened doors to use the low price and abundant liquid nitrogen as the refrigerant and boosted the applications of HTS materials. It is also possible to reduce the distance between the room temperature samples and the HTS sensors. Therefore, our magnetic biosensor uses HTS SQUID sensors.

Fig. 3.5 (a) illustrates a dc SQUID and its typical current-voltage characteristics in external applied magnetic flux at two extreme cases of integer flux quantum, $(n)\Phi_0$, and half-integer flux quantum, $(n+1/2)\Phi_0$. The magnetic flux quantum is defined by the Plank constant and the charge of the electron and is equal to, $\Phi_0 = h/2e = 2.068 \times 10^{-15}$ Wb. The SQUID is biased with the bias current slightly exceeding the critical current of the SQUID where a dc voltage appears across the junctions. The applied external flux creates a phase difference across the Josephson junctions. The total current is the sum of the critical currents in the two junctions. As a result, the total critical current of the SQUID depends periodically on the applied magnetic flux. When the applied flux reaches half a flux quantum, $\Phi = \Phi_0/2$, the total critical current reaches its minimum. As the external flux increases to an integer number of flux quanta, the critical current reaches its maximum. The voltage drop across the SQUID in turn swings between the two extreme cases as a function of external flux with a period of Φ_0, Fig. 3.5 (b). SQUID is therefore a flux-to-voltage transducer and the maximum response to a small change in the applied flux is obtained where the flux-voltage transfer function $V_\Phi \equiv |(\Delta V/\Delta\Phi_{ext})_{I_b}|$ is maximum.

There is a wide range of input circuits that can be coupled to the SQUID for various applications. In order to measure magnetic fields, a flux transformer pick-up loop configured as a magnetometer or gradiometer is coupled to the SQUID. Both the SQUID magnetometer and gradiometer are only sensitive to the variation of the magnetic field rather than measuring the absolute field strength. For our biomagnetic measurements, the SQUID sensor should operate outside a MSR in a homogeneous magnetic field in the vicinity of the SQUID. Furthermore, the first order field gradient term decays slower than the higher terms

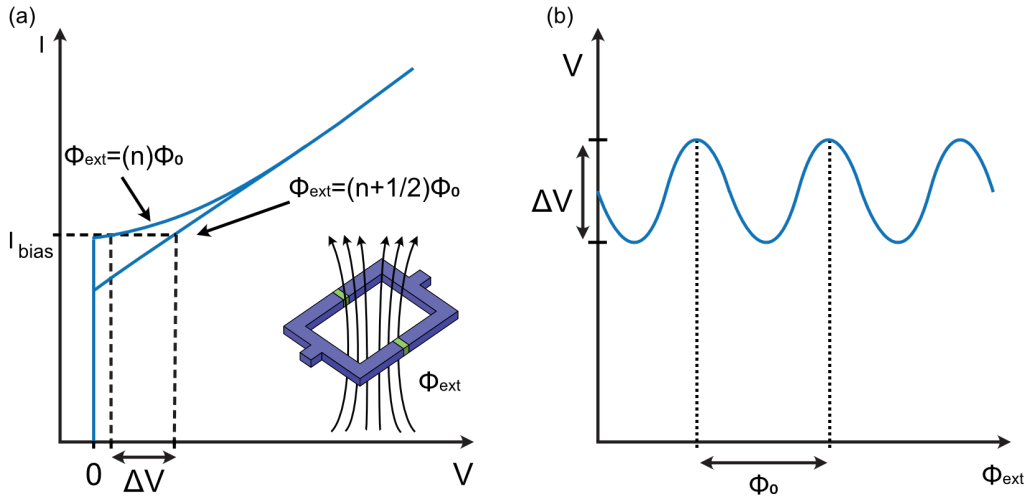

Figure 3.5: (a) Schematic of a dc-SQUID with two Josephson junctions interrupting the superconducting ring and the current-voltage characteristics of the SQUID in a integer ($(n)\Phi_0$) and half-integer ($(n+1/2)\Phi_0$) multiples of external applied flux quantum. (c) Voltage versus applied external flux dependency of the SQUID for an applied constant bias current.

with the distance from the magnetic sample. Therefore, the first order gradiometer layout is a more appropriate option for a sensor because it discriminates against distant magnetic sources and allows the magnetic field source close to the SQUID.

Two different layouts for the first order planar SQUID gradiometer are used in our experiments. Paper II uses the SQUID gradiometer I as shown in Fig. 3.6 (a) and Paper III and IV use the gradiometer II layout illustrated in Fig. 3.6 (b). The differences in the two gradiometers are minor. The baseline of the gradiometers, connecting the center of the two superconducting pick-up loops, is 3.6 mm. The screening currents induced by the external magnetic field in each of the two pick-up loops of a gradiometer cancel each other in the centerline of the loop. The SQUID is placed in the center of the middle line. The SQUID is directly connected to the pick-up loops and therefore can sense only the difference in magnetic flux in them. In both layouts, the SQUID is made from bicrystal grain boundary junctions in the YBCO film. The SQUID gradiometer sensors are fabricated in house and the fabrication technology is comprehensively described in earlier work [103]. The SQUID is operated in a so-called flux locked loop (FLL) due to its nonlinear voltage-flux response. The operating of the SQUID is outside the scope of this thesis,

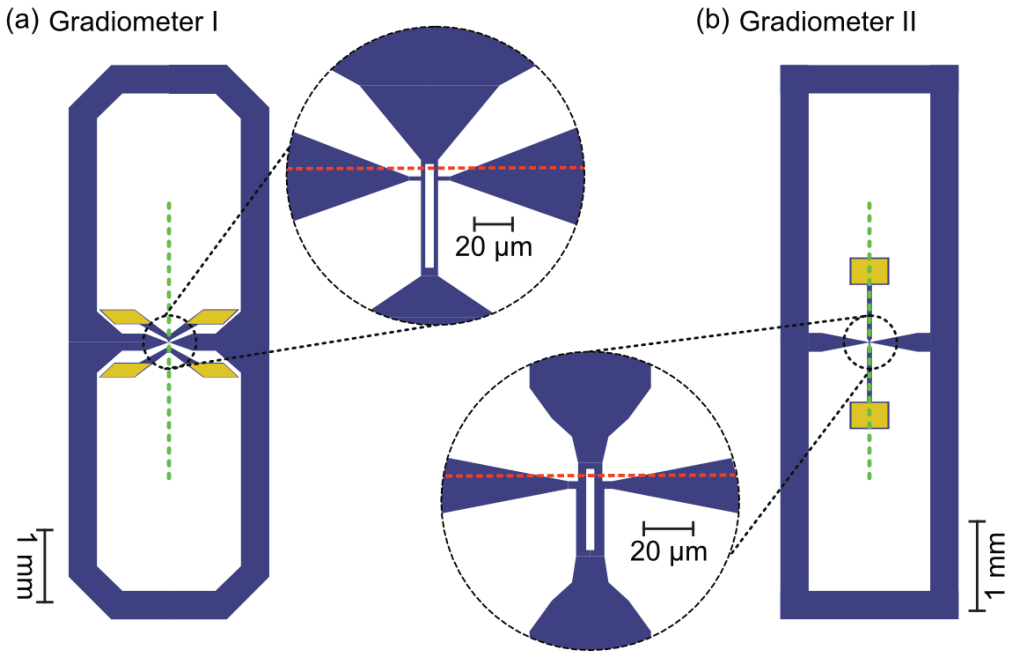

Figure 3.6: The layout of two fabricated SQUID gradiometers. (a) The gradiometer I was used in Paper II and has a 3.6 mm baseline. The widths of the pick-up loops are 400 µm. The SQUID loop has 4 µm wide strip lines, and the length and width of the slit are 50 µm and 3 µm, respectively. (b) The gradiometer II also has a 3.6 mm baseline and was used in paper III & IV. The widths of the pick-up loops are 400 µm. The SQUID loop has 3 µm wide strip lines, and the length and width of the slit are 42 µm and 3 µm, respectively. The red and green dashed line indicates the bi-crystal grain boundary and the baseline of the gradiometers, respectively. The grain boundary creates the Josephson junctions in the superconducting SQUID loop.

and an interested reader is referred to the SQUID handbook [104].

3.3.2 Liquid nitrogen cryostat

To operate the SQUID gradiometer sensor, it should be cooled down below the YBCO superconducting transition temperature of about 93 K. Therefore, the SQUID gradiometer sensor should be operated inside a LN_2 cryostat or any other suitable cooler that provides operation temperature below YBCO transition temperature. The lower operating temperature is preferable because higher level of noise is induced close to the transition temperature of the superconductor due to higher thermal noise, and fluctuations in SQUID parameters. The cryostat is made in-house from nonmagnetic materials. The sensor chip sits on a sapphire rod in direct contact with the liquid nitrogen. The liquid nitrogen reservoir is made out of fiberglass and is thermally decoupled from the envi-

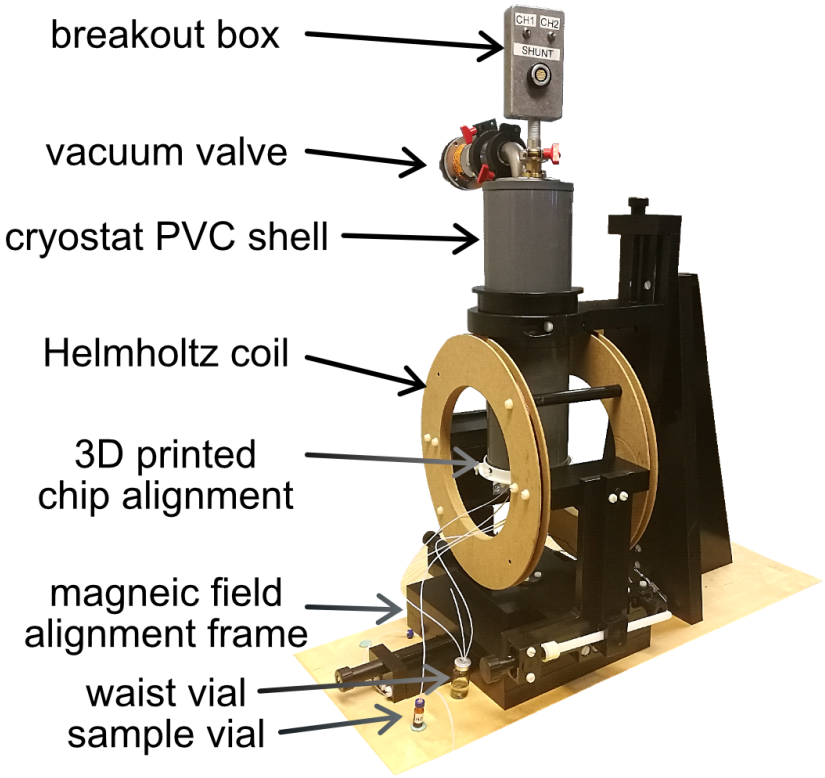

Figure 3.7: A photograph of the home-built liquid nitrogen cryostat. The SQUID is located behind the 250 µm thick sapphire window and the Helmholtz coil is aligned so that the SQUID is at the center of the coil with highest field homogeneity.

ronment by vacuum. A 250 µm thick sapphire window on the polyvinyl chloride (PVC) vacuum jacket separates the 77 K vacuum enclosed environment of the SQUID sensor from the room temperature environment. The distance from the sensor to the top of the sapphire window is less than 1 mm to allow better coupling between the magnetic samples and the superconducting pick-up coils of the gradiometer. A Helmholtz coil with a radius of 15 cm is used for producing a homogeneous magnetic field. The Helmholtz coil uses a movable frame to manually align the external magnetic field to minimize the coupling between the excitation field and the pick-up loops of the SQUID gradiometer. Fig. 3.7 shows a picture of the home-built liquid nitrogen cryostat setup. A schematic cross-section view of the cryostat is illustrated in Fig. 3.4.

3.3.2.1 Noise properties of the SQUID sensor in liquid nitrogen cryostat

The flux noise of the SQUID gradiometers cooled down using the LN_2 cryostat is measured inside the MSR. Fig. 3.8 shows the spectral density of the flux noise, $S_\Phi^{1/2}$ of gradiometers I and II which is given by the spectral density of the voltage noise, $S_V^{1/2}$, across the SQUID:

$$S_\Phi^{1/2} = S_V^{1/2}/V_\phi^2 \tag{3.2}$$

where the V_ϕ is the transfer function of the SQUID which is about 1 and 2 V/Φ_0 for gradiometer I and II. The best white noise levels achieved for gradiometer I and II are 12 $\mu\Phi_0/\sqrt{Hz}$ and 4 $\mu\Phi_0/\sqrt{Hz}$, respectively. The equivalent magnetic field noise of the SQUID gradiometer sensors can be extracted from the flux noise density by dividing it with the effective area, A_{eff}, of the gradiometer:

$$S_B^{1/2} = S_\Phi^{1/2}/A_{eff}. \tag{3.3}$$

The effective area of a gradiometer is difficult to calibrate experimentally, but assuming negligible SQUID effective area it can be approximated by $A_{eff} \approx L_c \frac{A_p}{2L_p}$, where L_c is the coupling inductance between the pick-up loops and the SQUID, A_p is the effective area of the pick-up loops, and L_P is the inductance of the pick-up loops [105]. The magnetic field noise of the gradiometer I and II are about 1 $pT/\sqrt{Hz}$ and and the gradient resolution is approximately: $S_G^{1/2} = S_B^{1/2}/b = 2.8\ pT/cm\sqrt{Hz}$, where b is the baseline of the gradiometer ($\approx$ 3.6 mm for both gradiometers). The $1/f$ noise, which is due to critical current fluctuations, is efficiently suppressed by operating the SQUIDs in bias reversal mode. This is important as the operating frequency window in our measurements is between 1 and 3000 Hz.

3.3.3 Two stage Joule–Thomson micro-cooler

Using LN_2 for cooling the SQUID sensor is an obstacle in realizing a POC diagnostics. LN_2 is not available in many places, especially remote areas where POC diagnostics is needed. It also requires access

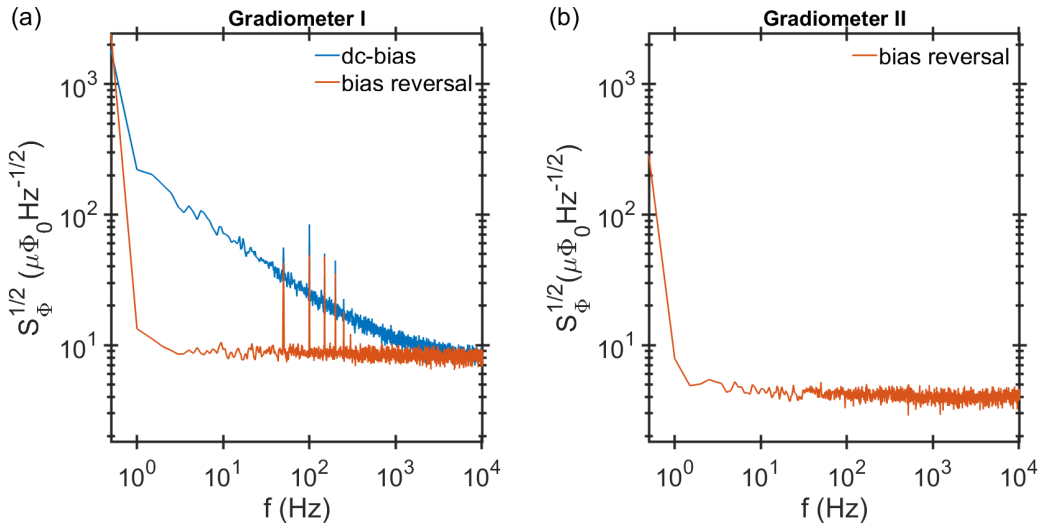

Figure 3.8: Spectral density of magnetic flux noise of the gradiometer I (a) and gradiometer II (b) are measured inside a MSR. The blue curve in (a) is measured using dc-bias and shows high $1/f$ noise. This $1/f$ noise is due to critical current fluctuations and is suppressed by using bias reversal as can be seen in the red curve.

to providers with facilities for production and delivery of the LN_2, and training of the operators for handling it. To eliminate the use of LN_2 and to provide an easy operation of the SQUID sensor, we have used a micro-cooler system based on a commercial desktop CryoLab unit from DEMCON Kryoz (`www.demcon-kryoz.nl`). It uses micro electro mechanical systems (MEMS) based Joule-Thomson coolers. The cold stage is made of a silicon wafer with microchannels where high-pressure gas flows to a flow restriction where it undergoes a Joule-Thomson expansion to low-pressure side and usually changes its phase to a liquid. The liquefied gas then evaporates by absorbing heat from its surroundings, producing low-pressure gas [106]. The CryoLab is an open-cycle system and contains a two-stage MEMS micro-cooler utilizing a high-pressure nitrogen gas (95 bar; ultra-high purity grade, 99.999%) from a commercial gas cylinder. Fig. 3.9 (a) shows the time dependency of the cold stage temperature when it is cooled from room temperature to the base temperature of 78 K. It is quite fast and reaches the base temperature of 80 K in about 30 min.

3.3.3.1 Noise properties of the sensor cooled with the micro-cooler

We have successfully operated the SQUID gradiometer for the first time in a two-stage MEMS based micro-cooler. The magnetic flux noise of

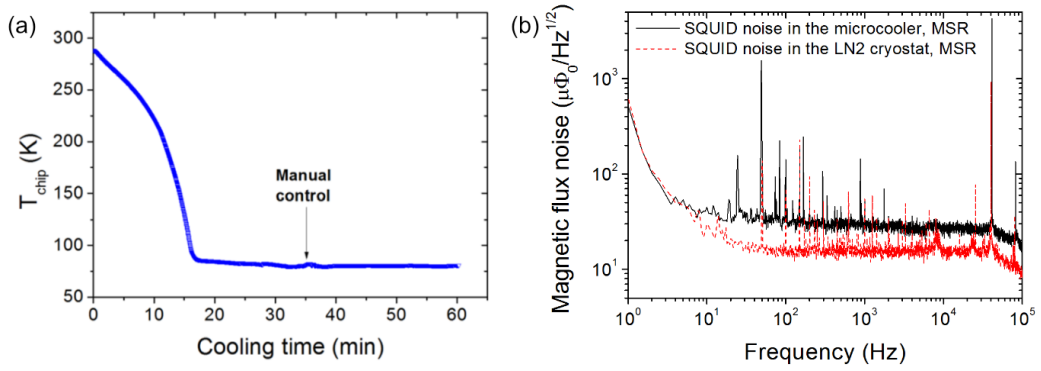

Figure 3.9: (a) Temperature of the cold tip of the micro-cooler as a function of time during a cool down from ambient temperature. The tiny bump indicates the point where the pressure regulation was switched to manual mode. (b) Spectral density of magnetic flux noise of the SQUID gradiometer cooled with micro-cooler (solid black line) and a liquid nitrogen cryostat (red dashed line) inside the MSR. Adapted form paper I.

the SQUID gradiometer cooled down with the micro-cooler is measured inside the MSR. Fig. 3.9 (b) shows the spectral density of the magnetic flux noise of the SQUID gradiometer. The micro-cooler was powered from an external dc power supply to eliminate various power-line cycle noise contributions in the vicinity of the SQUID sensor. The spectral noise density of the same sensor which was cooled in the LN_2 cryostat is also plotted in the same figure for comparison. The low-frequency peaks below 20 Hz are due to either electromagnetic noise from the membrane pump or vibrations in the nitrogen gas flow through the micro-cooler. The higher white noise level of the sensor in the micro-cooler may be due to the combination of errors in the calibration of the SQUID transfer function, different configurations in the feedback circuits and the higher resistance of the connecting manganin wires (all SQUID connection wires are from copper in the LN_2 cryostat). The higher resistance of the connecting wires contributes to the total noise of the SQUID.

Overall, the magnetic flux noise of the SQUID gradiometer is largely unaffected by the micro-cooler setup. This is promising for the stable operation of SQUID sensor without using LN_2. Further optimization is required to implement the micro-cooler in real field applications. This includes the elimination of additional wire resistance and the noise originating from the miniature membrane pump in the control unit by introducing a proper magnetic shielding between the pump and the sensor. The system should also be developed as a closed-cycle unit to reuse the

low-pressure gas and eliminate the supply of external gas cylinders.

3.3.3.2 Ac susceptibility measurements in the micro-cooler

We have also performed ac susceptibility measurement on MNPs using a SQUID gradiometer sensor cooled in the micro-cooler. Fig. 3.10 (a) is the complete setup with the home-built poly(ethylene terephthalate) (PET) vacuum housing and the Helmholtz coil for magnetic excitation. The Helmholtz coil is mounted on an alignment frame to minimize the coupling of the excitation field into the SQUID gradiometer loops. Fig. 3.10 (b) shows the real and imaginary components of ac magnetic susceptibility measurement from 100 nm streptavidin-coated MNP (1 mg/mL). During these measurements, the setup was cooled down and operated outside the MSR. These results show the feasibility of operating the SQUID without LN_2 in an unshielded environment and demonstrates the possibility of ac magnetic susceptibility measurements on the micro-cooler device. There are, however, some drawbacks that require modifications of the system. The SQUID sensor in the micro-cooler has higher white noise levels than in the LN_2 cryostat, Fig. 3.9 (b). This affects the sensitivity of the ac magnetic measurements in the micro-cooler compared to the LN_2 cryostat. The cold fingers are gold plated, and the ac excitation magnetic field from the Helmholtz coil induces eddy currents which are picked up by the sensor. The SQUID gradiometer should also be shielded as environmental magnetic noise disturbs the operation of the SQUID and, causes trapped flux inside the superconducting loops which requires warming up the SQUID sensor.

3.3.4 Microfluidics

Gradiometers are not sensitive to the distant sources. To measure the magnetic signals from the MNP samples, they should be located close to the gradiometer sensor. The implementation of the microfluidic channels in our biosensor provides control of the volume and geometry of the MNP solution. Microfluidics also facilitate the sample handling and later implementation of lab-on-a-chip technology. We ensure a maximized coupling by minimizing the distance between the microfluidic channel and the pick-up loops of the gradiometer sensor. This allows higher signal levels from lower MNP concentrations and therefore, increases

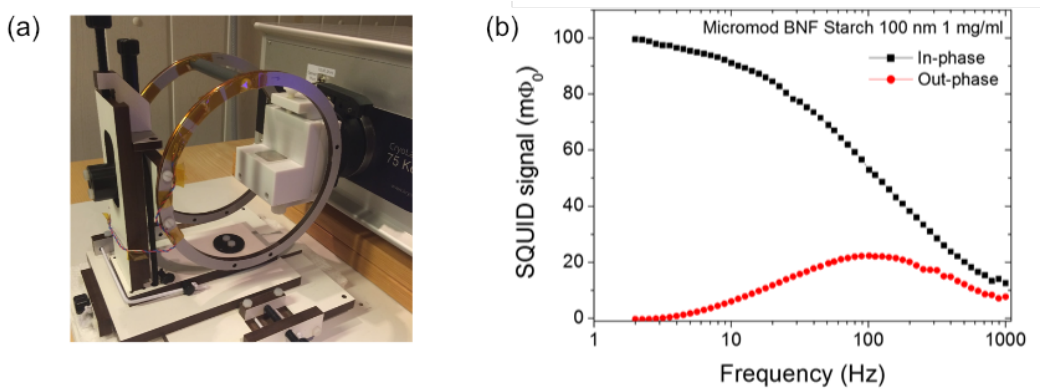

Figure 3.10: (a) A photograph of the complete system with its PET vacuum chamber and Helmholtz coil for magnetic excitation. The vacuum chamber has sapphire window of 0.25 mm thickness that provides access to the sensor and separates the cold stage from the room temperature environment. (b) Ac magnetic susceptibility of 100 nm MNP (1 mg/mL) versus the excitation frequency measured by SQUID gradiometer cooled down using the two stage micro-cooler.

the sensitivity of the whole assay to the RCPs. Appropriate alignment of the microfluidic channel with respect to the gradiometer sensor is also crucial for achieving maximum sensitivity to the MNP material. Therefore, a 3D-printed alignment frame which allows moving of the microfluidic chip in the X-Y plane of the sapphire window above the SQUID is mounted on the cryostat. A peristaltic pump connected to the sample vial allows pumping a small sample volume to the microfluidic channel for measurement.

Different materials can be used to fabricate microfluidic devices such as silicon, glass, and poly(dimethylsiloxane) (PDMS). We have chosen PDMS for our microfluidic chip for its fast, easy and cost-effective fabrication process. It is non-toxic, biocompatible, durable, flexible, and easy to handle, which makes it a great candidate for future POC developments [107]. PDMS devices are fabricated using soft lithography [108]. There are different methods to fabricate the master mold for casting replicas, such as photolithography, wet etching, wet/dry silicon etching, etc. Since the microfluidic devices being used here are rather simple and have large features, precision machining has been used to fabricate the master molds for the microfluidic devices. The main advantage of this technique is the fast transfer of a computer aided design (CAD) into a finished device. The structure of the channel is precisely machined into a

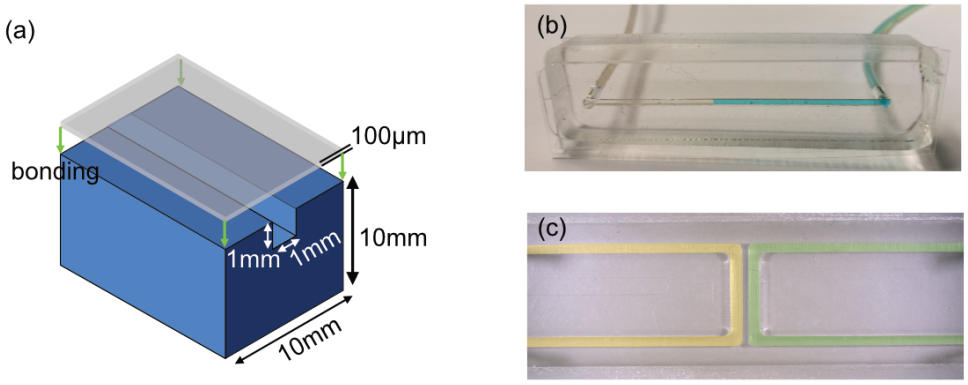

Figure 3.11: (a) The dimensions of the microfluidic channel, and photographs of completed (b) single channel, and (c) double-channel PDMS chips enclosed by bonding a 100 µm thin PDMS cap layer.

master aluminum piece, and many copies of the device are made from the same mold with good accuracy using the elastomer PDMS. Fig. 3.11 (a) shows the dimensions of the microchannel with 1×1 mm^2 channel cross-section and photographs (b) and (c) of the two completely fabricated chips used in our experiments with single and double channels.

The molding creates a PDMS replica with only three walls. Therefore, the channel has to be sealed separately. Since the magnetic samples should be as close to the sensor as possible, a thin layer of PDMS is used. A 100 µm thin layer is spin-coated on a silicon wafer and heat cured. Then the capping layer and the PDMS replica are put together to seal the channel since surface adhesion of the PDMS is sufficient to create a good contact. To make sure we have a tightly enclosed channel that does not leak under pressure, the two surfaces of the PDMS and the capping layers are primed in oxygen plasma before they are brought into contact. This process increases the bonding strength and can lead to a permanent bond between the two by forming covalent bonds [109].

3.4 Calibrating the setup with MNPs

Here, we present the ac magnetic susceptibility measurement of the 100 nm MNPs. The results are presented according to the kind of microfluidic chip used (single channel or double channel) and the alignment of the SQUID gradiometer in the magnetic field (parallel or perpendicu-

lar to the baseline of the gradiometer). All the following measurements are carried out using the LN_2 cryostat.

3.4.1 Single channel microfluidics

In this configuration, the baseline of the gradiometer is in-plane and parallel to the external magnetic field line. The single-channel microfluidic chip which carries the MNPs has the maximum coupling to the two pick-up loops of the gradiometer if it is placed above the middle line of the gradiometer. Fig. 3.12 (a) is a schematic illustration of this configuration and shows the evaluated magnetic flux threading the gradiometer loops using a simple model considering the MNPs as point-sources and randomly distributing them in the volume of the microfluidic chip [110]. Aligning the channel with the upper or the lower lines of the gradiometer (parallel to the middle line of the gradiometer) would result in coupling of magnetic flux from the sample to only one of the two pick-up loops. Fig. 3.12 (b) shows a photograph of the single-channel microfluidic chip aligned above the middle line of the gradiometer which gives the maximum coupling between the MNP sample in the microfluidic chip and the gradiometer sensor.

The in-phase and out-of-phase components of the SQUID signal acquired from streptavidin-coated MNPs of various concentrations diluted in PBS versus the excitation field frequency are reported in Paper II. The samples are measured at the maximum excitation field strengths of 40 µT. The imaginary part of the ac magnetic susceptibility has its peak amplitude at the Brownian relaxation frequency at around 80 Hz. The amplitude of both real and imaginary parts of the ac susceptibility decreases with decreasing the concentration of MNPs. There is no frequency shift in the peak position of the imaginary part due to magnetic field strength or MNP concentration. This indicates that we are in the low field region, and there are no magnetic interactions between MNPs [111].

To extract the MNP sensitivity, the peak amplitude of the imaginary component of the susceptibility for different concentrations of the MNP is plotted against the number of particles. The number of MNPs in each concentration is estimated from the known number of particles per

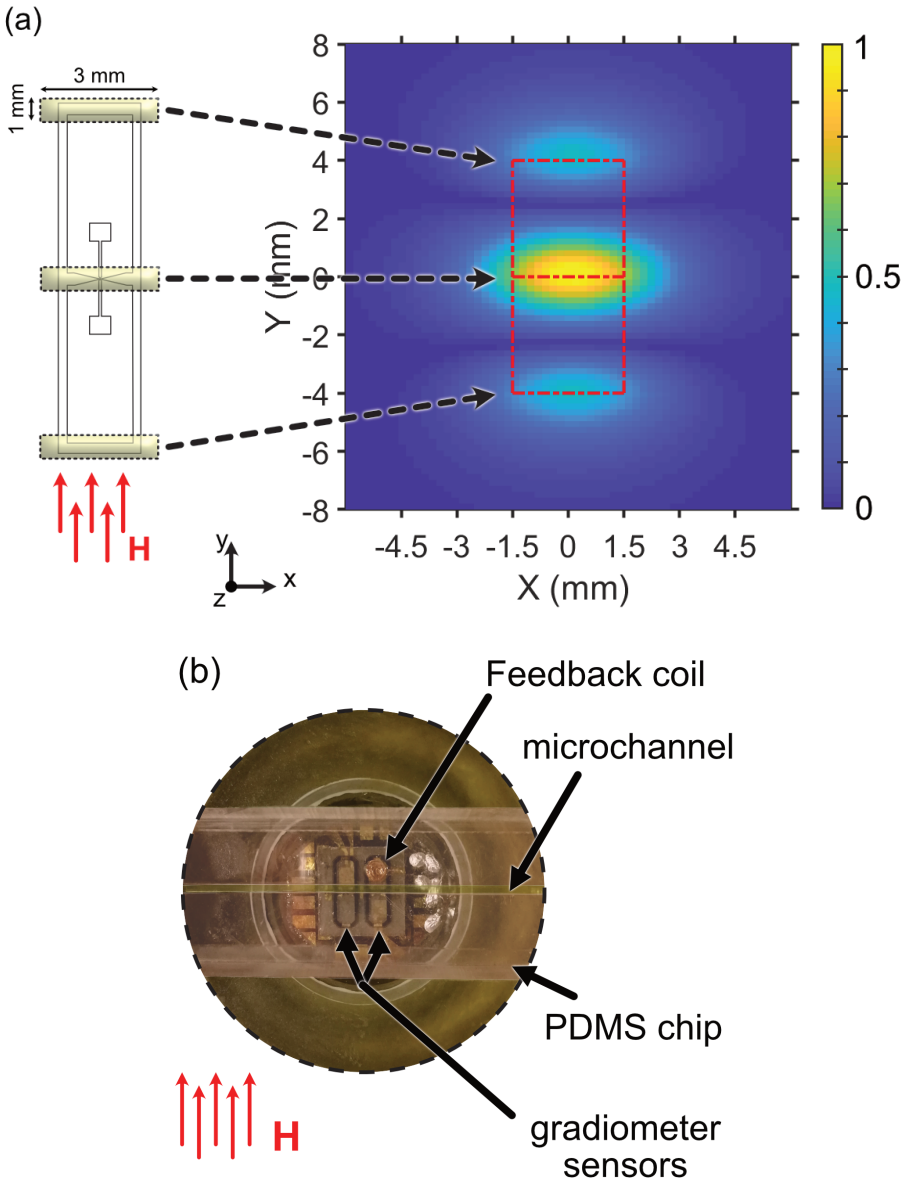

Figure 3.12: (a) A schematic illustration of the channel alignment with respect to the SQUID gradiometer sensor and simulation of the normalized absolute total magnetic flux threading the gradiometer loops. The channel has the cross-section of $1 \times 1\ mm^2$ and length of 3 mm in dimensions and particles are randomly distributed in its volume. The center of the defined channel sweeps the x-y plane of the gradiometer at a constant distance of 1.1 mm and the resulting flux threading the gradiometer loops at each point is evaluated and normalized. (b) A photograph of the aligned channel on the gradiometer sensor. The field line is in-plane and parallel to the baseline of the gradiometer. As indicated by the simulations, the maximum signal is realized by aligning the microchannel above the centerline of the gradiometer in this configuration. Adapted form paper II.

unit volume which according to the datasheet of the MNP system is 6.0×10^{12} particles per ml in a 10 mg/ml concentration. Fig. 3.13 shows the linear relation between the amplitudes of the peak imaginary component and the number of MNPs measured at the magnetic strength of 40 µT and 250 µT. The vertical axis corresponds to the SQUID output signal in the units of magnetic flux quanta. The extrapolation of the linear dependence to the measured noise floor of the SQUID gives the estimation of the theoretical magnetic content sensitivity of our system. For gradiometer I the white noise is 1.2×10^{-5} $\Phi_0/\sqrt{Hz}$ and the corresponding magnetic content sensitivity of this sensor at excitation field strength of 40 µT is 1.5×10^6 MNPs/$\sqrt{Hz}$ or 4.3×10^{-10} $emu/\sqrt{Hz}$ in magnetic moment ($1\ emu = 10^{-3}\ Am^2$). This is equivalent to 2.5 ng of MNP. For the excitation field strength of 250 µT, the magnetic content sensitivity is 1.2×10^5 MNPs/$\sqrt{Hz}$ or 2.15×10^{-10} $emu/\sqrt{Hz}$ in magnetic moment. This is equivalent to 0.25 ng of MNP, c.f. Fig. 3.13. This value is an important figure of merit as it determines the sensitivity of the magnetic sensor. These are excellent values in terms of magnetic moment sensitivity compared to other commercial available systems such as vibration-sample magnetometers (LakeShore Cryotronics) with 150×10^{-10} $emu/\sqrt{Hz}$ and DynoMag (RISE Acreo) with 80×10^{-10} $emu/\sqrt{Hz}$.

Increasing the strength of the magnetic field increases the magnetization of the MNPs and results in higher signals from the samples. Therefore, the sensitivity of the sensor to the magnetic material increases. At high strength of the magnetic field the precise alignment of the SQUID gradiometer in the field becomes crucial as any misalignment would results in large unwanted coupling of the excitation field into the pick-up loops of the gradiometer. The strength of the field should be chosen so that it is well below the saturation magnetization of the MNP system. It is necessary to ensure the linear dependency of the magnetization of the MNP system as a function of the excitation field. The intrinsic saturation magnetization of the 100 nm BNF starch MNP system is 370 kA/m (0.46 T) with linear field range of ±1 kA/m (±1 mT) [48], which are well above the highest amplitude of the magnetic excitation field applied here (250 µT).

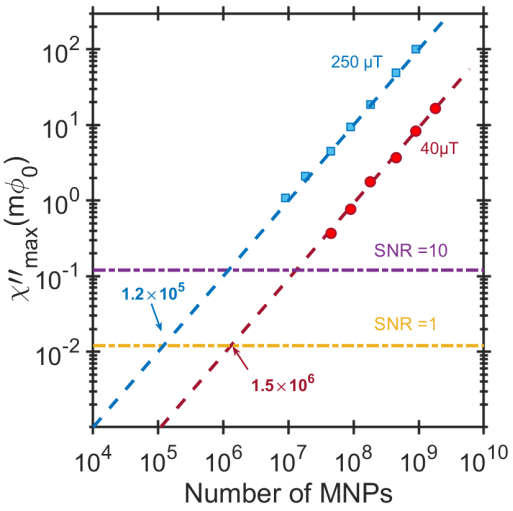

Figure 3.13: The peak amplitude of the imaginary component of the ac magnetic susceptibility signal at around 80 Hz as a function of number of MNPs at maximum excitation field amplitudes of 40 and 250 µT. The dashed line is a linear curve fitted to the data with a regression coefficient of 0.99. The yellow and purple dash-dotted lines correspond to the SNRs of 1 and 10 in gradiometer I.

3.4.2 Differential ac susceptibility

When the field lines are aligned in-plane and perpendicular to the baseline of the SQUID gradiometer, the maximum coupling of the stray field from the MNPs to the gradiometer loops is achieved by placing the microfluidic chip with the MNP system under investigation on the sidelines of the gradiometer which are parallel to the baseline, Fig. 3.14. In this geometry, the screening current produced by magnetic flux from the magnetic fluids in a single channel chip is subtracted in the middle line of the gradiometer where SQUID sensor is situated. Since the gradiometer subtracts the signals from its two pick-up loops, using the single-channel microfluidic will give zero signal. In this case, the double-channel microfluidic chip, which has two independent microfluidic channels integrated into a single PDMS chip, is used for sample handling. The channels are aligned parallel to the baseline above one of the two sidelines of the gradiometer loop in a way that the PDMS wall that separates the two channels is centered parallel to the middle line of the gradiometer sensor, Fig. 3.14. In this configuration, the stray fields from the MNP sample in each channel is only coupled to one of the two loops of the gradiometer.

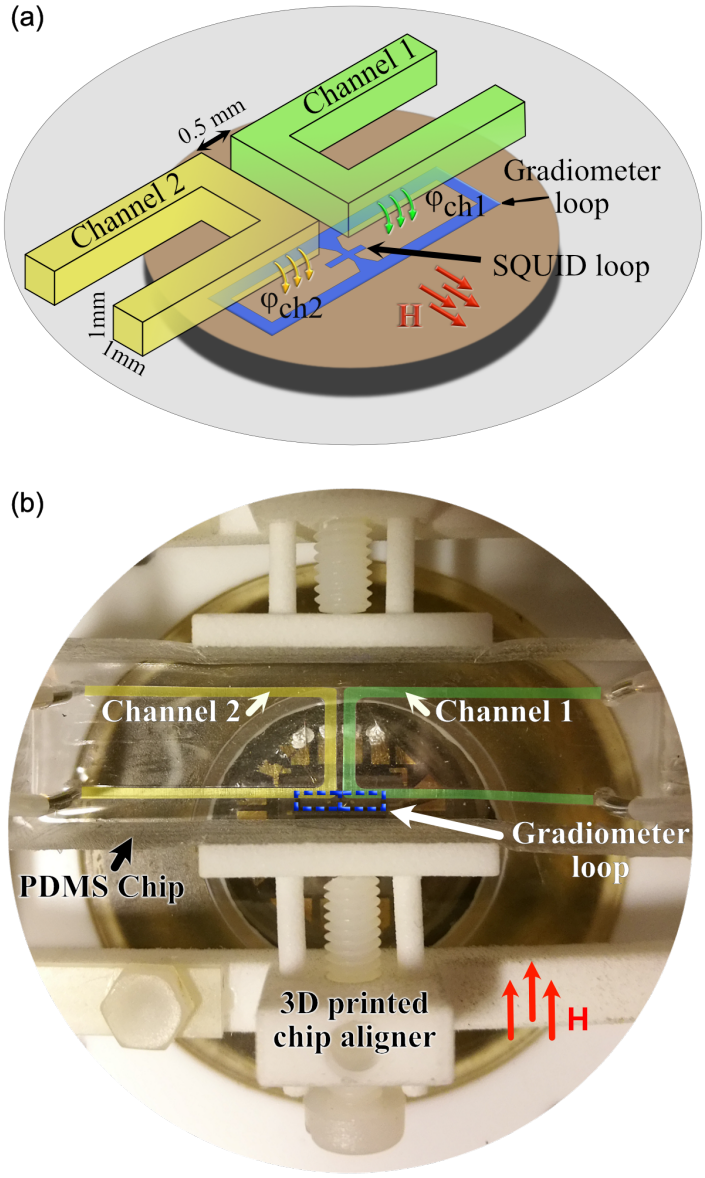

Figure 3.14: (a) Schematic illustration of the configuration of the two microfluidic channels above a 1st order planar gradiometer SQUID sensor. An ac magnetic excitation field (H) is applied to the channels, in-plane with the sensor chip and perpendicular to the baseline so that the SQUID is insensitive to it. In this configuration, the magnetic fluxes produced by the MNPs in each channel is only coupled to one of the individual pick-up loops of the gradiometer. (b) A top view photograph of the microfluidic chip aligned above the SQUID sensor; the dashed blue line indicates the SQUID gradiometer and the channels are highlighted in yellow and green. Adapted from paper III.

Fig. 3.15 (a) shows the real and imaginary components of the ac susceptibility from 100 nm particle size MNP samples filling either Ch. 1 or Ch. 2 of the PDMS chip. The measurements are carried out when the channels are already filled with individual samples, and the sample solutions are not flowing. Since each channel is coupled to only one single pick-up loop of the gradiometer, the magnetic ac susceptibility signals from Ch. 1 is opposite in sign compared to that of Ch. 2. The opposite signs of the signals from Ch. 1 and Ch. 2 makes it possible to perform differential ac susceptibility measurements between the two individual samples in Ch. 1 and Ch. 2. In this configuration, the differential readout is capable of canceling signals from two identical magnetic samples filled in both channels. The blue circles in Fig. 3.15 (a) shows the magnetic ac susceptibility responses from the 100 nm MNPs filling both channels. The response signal is approximately zero and matches well with the manually subtracted signals from the individually-filled channels. Fig. 3.15 (b) shows the differential measurement and the manually subtracted ac susceptibility signals from individual channels and indicates lower errors in the differential measurement. The similarity of the two ac susceptibility responses shows that the measured ac susceptibility signal is a linear superposition of the positive and negative signals from Ch. 1 and 2. When measuring two different samples filling Ch. 1 and 2, the expected result is proportional to the relative difference in the ac susceptibility of the two samples which could, for example, be a result of a relative difference in the particle size distributions and/or magnetic particle concentration. The differential signal is less than 1% of the amplitude of the signals from the individual channels. The standard deviations in the differential measurement signals are smaller compared with manually subtracted signals from individual channels and therefore gives a higher SNR.

In the next step, we calibrate the magnetic sensitivity of our readout system by measuring different concentrations of MNPs in one channel, while a control sample with a fixed MNP concentration is present in the other. The concentration of the control sample in Ch. 1 is 250 µg/mL, while test samples in Ch. 2 contain MNPs with concentrations ranging from 1 to 250 µg/mL. The results of the differential ac susceptibility for different concentration of MNPs in the test samples are reported

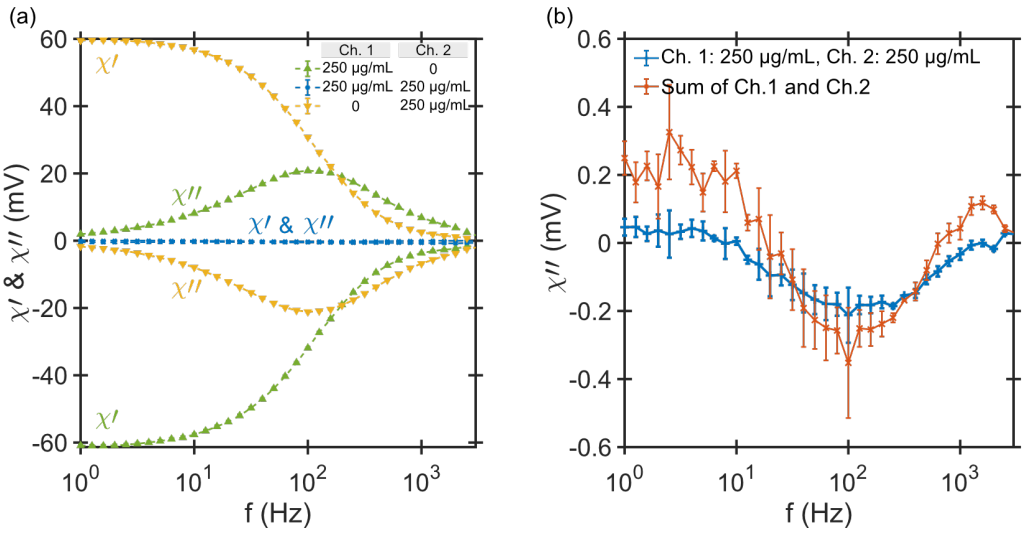

Figure 3.15: (a) The real and imaginary components of the ac magnetic susceptibility versus the frequency of the magnetic excitation field from 250 µg/mL MNP samples filling: only Ch. 1 (green triangles), only Ch. 2 (yellow triangles), and both channels (blue circles). The magnetic ac susceptibility signals from ch. 1 are opposite in sign compared to that of Ch. 2 due to the differential measurement setup. (b) The measured imaginary component of ac magnetic susceptibility, when both channels are filled, is plotted together with the sum of the signals from the individual channels shown in part (a). This magnetic ac susceptibility signal is considered the zero signal of the system and is $\approx$ 100 times lower in magnitude compared to the individual signals in Ch. 1 or Ch. 2. The summation of the magnetic ac susceptibility signals from the individual channels results in the same response as obtained from the measurement. Adapted from paper III.

in paper III. When the particle concentrations in the two channels are equal ($C_{Ch.1} - C_{Ch.2} = 0$), even if the particle concentration in each channel is rather high, the differential susceptibility measurement gives a zero-response signal.

On the other hand, when the concentration of the test sample becomes significantly small as compared to that of the control sample (i.e., when $C_{Ch.1} - C_{Ch.2} \approx C_{Ch.1}$), the susceptibility signal saturates to that of the control sample. This saturation can be avoided by further increasing the concentration of the control sample. This would also extend the dynamic range of the differential readout. Therefore, the differential readout is highly sensitive to small differences between magnetic samples in the two channels. This is crucial for the realization of homogeneous magnetic assays that aim to have high dynamic range and at the same time detect low concentrations of target molecules .

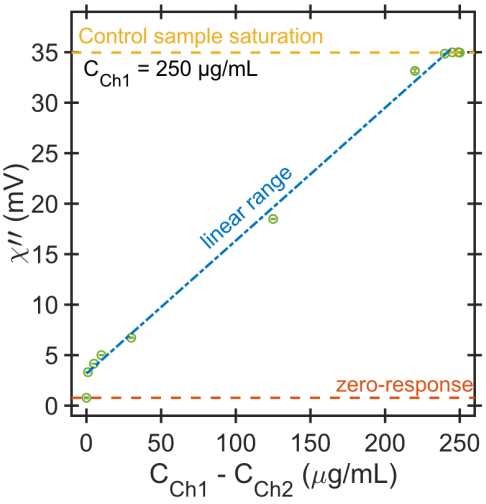

Figure 3.16: The amplitude of the imaginary component of the differential ac susceptibility peak at 100 Hz versus the difference in the concentration of MNPs in the two channels. When the difference in the two concentrations is large, the background magnetic signal makes it difficult to distinguish small differences in the test sample, and the imaginary susceptibility saturates to that of the control sample signal amplitude. The blue line indicates the linear range of operation and has a regression coefficient of 0.99 (excluding the zero-response and the saturation values). Adapted from paper III.

Fig. 3.16 shows the imaginary part of the differential ac susceptibility at the peak-amplitude frequency as a function of the difference in the MNPs concentrations in the two channels. Using this calibration curve, we can calculate the difference between the concentrations of MNPs in the two samples, assuming they have the same particle size distribution. The differential sensor signal is a linear function of the difference in the concentrations in the two channels. For samples with different particle size distributions, however, the full frequency response should be measured to obtain information about the difference in size distributions between the two samples.

CHAPTER 4

Quantification of rolling circle products (RCPs)

In this chapter, we quantify the RCPs by labeling them with MNP and measuring the ac magnetic susceptibility using the measurement setup described in the previous chapter. In the following experiments, plain particles (with no surface functionalization) and streptavidin-coated multi-core MNPs of 100 nm in size are used. The streptavidin-coated MNPs are functionalized with oligonucleotides by forming a streptavidin-biotin bond, and they are used for specific binding to our target analytes, namely the RCPs, See Appendix A. Several methods were introduced in Sec. 2.2.4 for quantification of target molecules using ac magnetic susceptibility measurements. First, we present and discuss the results for the turn-off detection approach, which are published in paper II. Then we focus on the turn-on detection of RCPs using the differential ac susceptibility measurement technique we have developed and was introduced in Sec. 3.4.2.

4.1 Turn-off detection of RCPs

To detect the final products of the RCA process (i.e., RCPs) they are magnetically labeled by functionalized MNPs of 100 nm in particle size, see Appendix A. To quantify the RCPs using magnetic reduction technique, two measurements are necessary: a reference measurement and a positive test measurement. The detection signal appears due to the presence of the target analyte (RCPs) in the positive test sample. This signal is a reduction in the peak amplitude of the imaginary component of ac susceptibility (compared to the reference signal) at a particular frequency. The ac magnetic susceptibility of the MNP labels reduces due to binding with the target analytes (i.e., RCPs), which are volume amplified for 60 min during the RCA process and have quite large hydrodynamic sizes. The reduction is either due to the increase of hydrodynamic size or clustering of a fraction of MNPs that are bound to the RCPs. This will, in both cases, separate the Brownian relaxation frequency of these formed complexes far away from the unbound MNPs.

A magnetic biosensor with high sensitivity and specificity requires a colloidally stable MNP system. The colloidal stability is particularly necessary and essential in the turn-off detection because fluctuations in the reference signal could impede the sensitivity of the biosensor or cause a false interpretation of the detection signal. While the particle system may be stable in its initial concentration and form, handling them using the microfluidic chips can affect the stability of the MNPs and induce signal variations. Therefore, we first investigate the colloidal stability of our MNPs before using them as labels for detection of RCPs. After establishing the colloidal stability of the MNP labels in the microfluidic channels, we quantify the RCPs using the turn-off detection approach.

4.1.1 Stability of MNPs in microfluidic channel

Measurements of the plain MNP (with no functional coating) in the microfluidic channel show that the particle system is quite stable and has no loss of signal over time or upon multiple filling and flushing of the microfluidic channel. The streptavidin-coated and oligonucleotide functionalized MNPs, on the other hand, show a loss of signal over time when they are measured inside the microfluidic channel. This loss of

signal might have different reasons, for instance agglomeration of the particles, sedimentation of the particles inside the channel, or binding of the MNPs to the surface of the PDMS channel. Since the reduction in the imaginary component of the ac susceptibility is taken as the detection signal when detecting the target analyte, any instability in the colloidal solution would cause an error in the measurement, particularly at low target concentrations.

In order to study the stability of the samples, we have measured the ac susceptibility of the streptavidin-coated MNPs with 100 nm median size and 1.0 mg/mL concentration inside the microchannel. Upon different fillings, the results showed no shift in the peak frequency of the imaginary component or broadening of the signal. Therefore, the hydrodynamic size of the MNPs did not change in the measurements time window. There is, however, some signal loss. To see the dynamical behavior of this signal loss, the real and imaginary parts of the ac susceptibility at a frequency close to the peak amplitude of the imaginary part were measured for 12 min. The data points were taken every second at around 63 Hz and are plotted against time in Fig. 4.1. Both components of the ac susceptibility show a continuous decrease with time for the streptavidin-coated MNPs. This loss of signal is more substantial and easily visible in measurements of multiple fillings of the same sample in the microfluidic channel as shown in Fig. 4.1 (b). In this experiment, the 100 nm streptavidin-coated MNPs in PBS buffer solution show a significant loss of signal after each refill. This constant decrease in signal with time is an issue that needs to be addressed if the particle system is to be used in the microfluidic channels. This also indicates that our measurement setup is sensitive to the MNP probe stability.

Slopes of the lines in Fig. 4.1 (a) define the rates at which the real and imaginary ac susceptibility decrease over time. For the streptavidin-coated MNPs in PBS, the real and imaginary components decrease at a rate of -1.12 µV/s and -0.75 µV/s, respectively. In other words, it takes 2.5 and 3 min for the real and imaginary components of the ac susceptibility to lose 1% of the original signal amplitude, respectively. The signal loss can be attributed to the streptavidin coating of the 100 nm MNPs. Streptavidin tends to bind to the surface of the PDMS channel

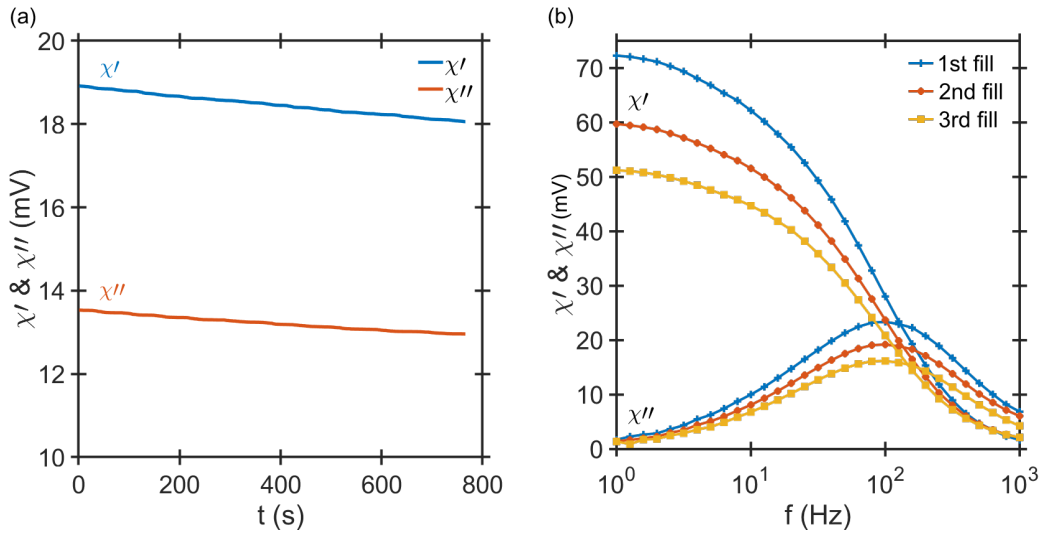

Figure 4.1: (a) The real and imaginary ac susceptibility as a function of time at a constant frequency of 63 Hz for streptavidin-coated MNPs (median size of 100 nm) in PBS. The sample was resting inside the channel during the whole measurement time. (b) Multiple filling of the same sample in the microfluidic channel and measurement of ac susceptibility shows that each time the sample is removed from the channel and filled back the signal levels drop substantially compared to the first fill.

[112] that results in the loss of the signal. This loss is at a much higher rate compared to the plain MNPs. The slope for both the real and imaginary component of the ac susceptibility from the plain MNPs is around 90 nV/s and positive. At this rate of change, it takes roughly 40 hours to affect the signal amplitude by 1%. We attribute this signal change to the shift in the calibration (background signal) in our setup.

One possible solution is to coat the microfluidic channel with biocompatible materials such as poly(ethylene oxide) (PEO) and poly(ethylene glycol) (PEG) to avoid nonspecific binding of the streptavidin-coated MNPs to the surface [113]. These processes are short term solutions and complicate the fabrication of the microfluidic chips. A simpler solution is to add polysorbate 20 (Tween-20) to the buffer solutions (i.e., PBS). Tween-20 is a non-ionic surfactant with a hydrophobic (the hydrocarbon chains) and hydrophilic (ethylene oxide units) functional groups. Adding the Tween-20 to the buffers at dilution of 0.05-0.5% helps to prevent nonspecific binding of the MNP to the walls and decreases the surface tension.

Fig. 4.2 (a) shows the time dependence of the real and imaginary ac

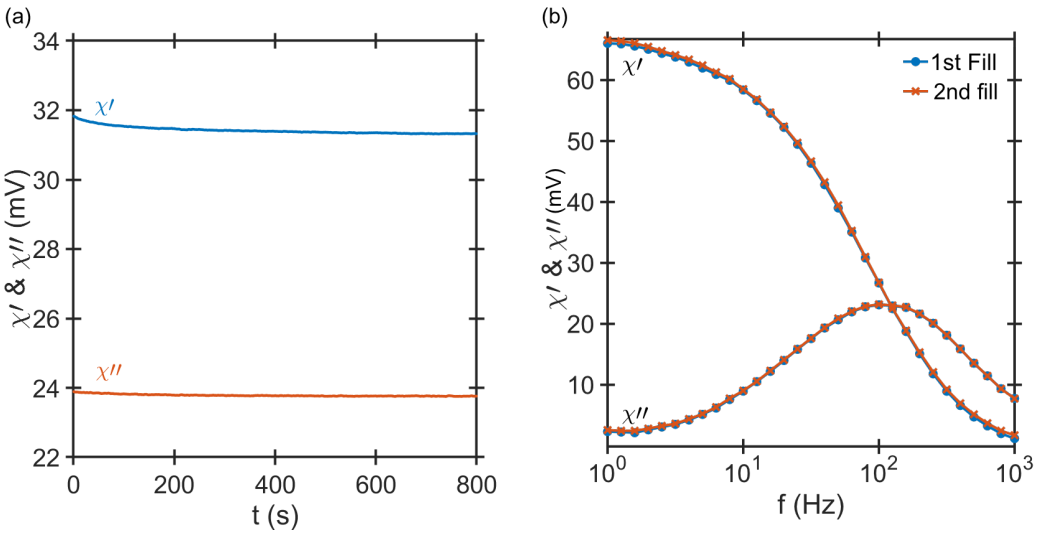

Figure 4.2: (a) Ac susceptibility measurement of 100 nm streptavidin-coated MNPs in only PBS buffer solution including 0.05% Tween-20 shows a slower rate in the drop of the signal amplitudes in the both components of the ac susceptibility signal. (b) Two consequent magnetic ac susceptibility measurements of the same sample in the microfluidic channel shows not drop in the ac susceptibility measurement after the refilling. The addition of 0.05% Tween-20 in the PBS buffer solution decreases the interaction of the MNP with the tubes and microchannel and loss of material.

susceptibility as a function of time at a constant frequency of 63 Hz for streptavidin-coated MNPs in PBS solution containing 0.05% Tween-20 in dilution. The real and imaginary components decrease at slower rates of -0.63 µV/s and -0.14 µV/s (compared to MNP dilutions in only PBS, Fig. 4.1), respectively. It therefore, takes at least 30 min to lose 1% of the imaginary component original signal amplitude. Fig. 4.2 (b) shows the positive effect of using Tween-20 in the buffer solution in multiple fillings of the same magnetic sample in the microchannel. The MNP in the PBS buffer containing 0.05% Tween-20 dilution shows no change in its peak amplitude due to refilling of the microfluidic channel. The same behavior is observed for streptavidin-coated MNPs with oligonucleotide tags. The addition of the Tween-20 provides us with a colloidally stable MNP system that is appropriate for turn-off/on detection of RCPs.

4.1.2 Measurement of RCPs

The RCPs of synthesized *Vibrio Cholerae* targets used in the following measurements are products of 60 min RCA amplification time, Sec. 3.1. The RCPs are labelled with 100 nm MNPs and different dilutions of

RCPs are prepared as positive test samples. The positive test samples contain RCPs ranging from 0 to 30 pM (picomole/L) and are measured in the frequency range of 1 to 3000 Hz. The results are reported in paper II. The negative control (NC) sample contains only MNP labels with mass concentration of 50 µg/mL (50 pM), and zero concentration (0 pM) of RCA. The imaginary ac susceptibility component for the NC sample reaches a maximum at around 63 Hz. The reduction in the peak amplitudes of the imaginary parts from the positive test samples compared to the amplitude of the NC sample is the detection signal in the turn-off detection scheme, c.f. Fig. 4.3. Due to large hydrodynamic volume of the RCPs, the MNP-RCP complex has its Brownian relaxation frequency at very low frequencies. Since the MNP are hybridized into the RCPs in positive test samples, the peak amplitude at the Brownian relaxation frequency of the free MNP is lower than in the NC sample without any RCPs. The amplitude of this signal reduction is directly related to the number of RCPs in the positive test sample.

We can also estimate the number of MNPs bound to each RCP in the positive test sample. Assuming constant effective particle magnetic moment, the peak amplitude of the imaginary component of ac susceptibility is proportional to the concentration of the MNPs [48], See Fig. 3.13. Thus, the signal drop at each concentration of RCP represents the number of MNPs bound to the RCPs in that test sample. We know the concentration of the RCPs in each test sample, C_{RCP}, and the initial concentration of the MNPs, C_{NC}. The estimated the number of MNPs per RCP, g, at each concentration of the test sample is therefore given by:

$$g = \frac{C_{MNP}^{bound}}{C_{RCP}} = \frac{(\chi''_{NC} - \chi''_{C})}{\chi''_{NC}} \times \frac{C_{NC}}{C_{RCP}} \tag{4.1}$$

where C_{MNP}^{bound} is the concentration of the bound MNPs, χ''_{C} is the peak amplitude of the imaginary susceptibility of test sample of concentration C, and χ''_{NC} is the peak amplitude of the imaginary susceptibility of the NC sample. We observe that g decreases from 3.6 to 1.3 as the RCP concentrations in the test sample increases from 1 to 30 pM. On average

we estimate 2 MNPs per RCPs which is close to what has been reported earlier using the DynoMag system [114] and transmission electron microscopy (TEM) for 130 nm MNPs [115]. We attribute the higher value of g at lower RCP concentration to the higher number of available MNPs in the test sample; 50 MNPs per RCP at 1 pM to 1.6 MNPs per RCP at 30 pM.

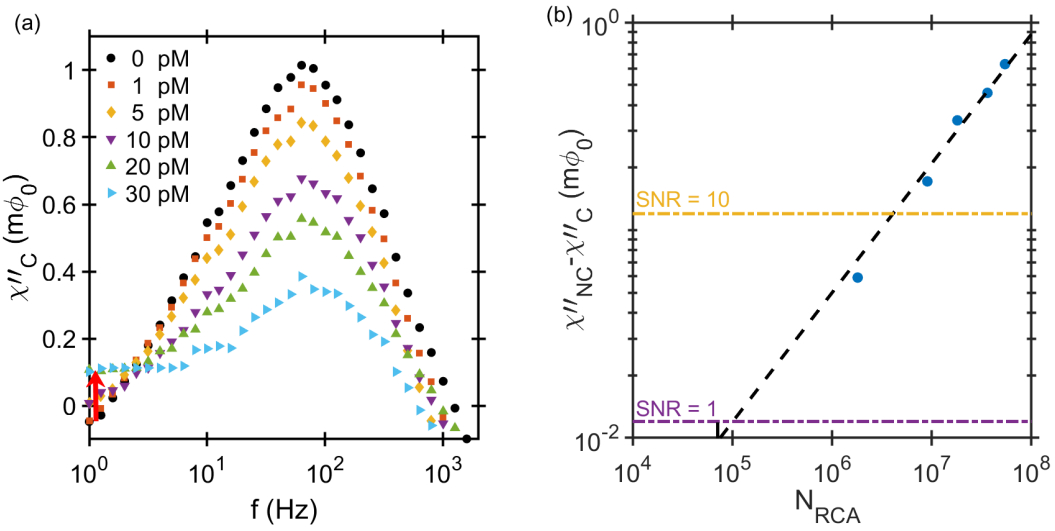

Figure 4.3: (a) The imaginary parts of the ac susceptibility as a function of excitation frequency for different concentrations of RCPs ranging from 0 (NC) to 30 pM in a total volume of 3 µL. The drop in the amplitude of both real and imaginary components of the susceptibility indicates the increase in the number of RCPs and fewer numbers of unbound MNPs in the solution. The red arrow shows a raise in the low frequency tail of the response with increasing RCP concentration. (b) The extinction signal ($\chi''_{NC} - \chi''_{C}$) for different concentrations of the RCPs at the peak frequency of 63 Hz as a function of the number of RCPs in each corresponding concentration. The linear extrapolation gives 1.0×10^5 RCPs as a theoretical limit of detection in a 3 µL sample volume at SNR = 1. Adapted from paper II.

The amplitudes of both the real part and the imaginary part continuously decrease with increasing RCP concentration. This decrease is due to binding of MNPs to RCPs and reduction of the number of free unbound MNPs in the solution as the RCP concentration increases. The 60 min amplification time is expected to result in rather large RCPs, typically 1000 padlock probe copies with about 1 µm final size. Therefore, the effective hydrodynamic volume of the MNP-RCP complex is also large and the corresponding Brownian relaxation frequency decreases well below 10 Hz (the Brownian relaxation frequency of the 1 µm RCA coils is about 0.4 Hz). However, It should be noted that the NTA measurements show that the RCPs tend to have a broader size distribution

with increasing amplification time. Furthermore, the sizes of the RCPs depend also highly on the ionic strength of the buffer solution (this is discussed more in paper IV). The increase in the imaginary part of the magnetic susceptibility signal below 10 Hz may be due to the appearance of a low-frequency peak, the red arrow in Fig. 4.3 (a). The low frequency peak is more pronounced for higher concentrations of RCA coils due to the greater ratio of MNP-RCP complexes to free MNPs. The turn-off detection signal, which is the extinction signal $\chi''_{NC} - \chi''_{C}$, at 63 Hz is plotted against the number of RCPs in Fig. 4.3 (b). The sensor signal is proportional to the RCP concentration (ranging from 1 to 30 pM), with experimental LOD of 1 pM. Extrapolating the linear dependence of extinction to the noise floor of the sensor corresponds to an estimated theoretical LOD of about 1.0×10^5 RCPs corresponding to 66 fM. The reported values assumes 100% success rate for the amplification process which has been shown to be about 22.6% [95]. This means the experimental LOD is nearly 5 times better than the reported values.

4.1.3 Comparison with other state-of-the-art biosensor methods

The commercial SQUID magnetometer (QD MPMS XL, Quantum Design) was initially used to measure the magnetic properties of the MNP labels and their binding reactions with RCPs implementing the turn-off detection approach [78]. Using RCA technique for amplification of target DNA molecule, the biosensor based on this magnetometer has achieved LOD of around 3.7 pM [78, 87]. This commercial system, however, is quite bulky, very expensive, and requires extensive magnetic shielding and cooling down to liquid helium temperature. Other magnetic sensor systems have also been used since for detection of magnetically labeled RCPs. Examples of such systems are commercial DynoMag system based on induction coils [114, 116], optomagnetic sensor based on blue-ray optical pick-up unit [117, 51, 118], anisotropic magnetoresistance sensor [119], and electron paramagnetic resonance [120]. Table 4.1 lists these biosensors and summarizes their performance for comparison. These systems have contributed to improving the performance of RCA based nucleic acid biosensors in terms of detection limit, operating temperature, magnetic shielding, price and compatibility for POC

diagnostics.

Although much effort is devoted to improving the sensitivity of these magnetic biosensors, the magnetic background signal from the unbound MNP in the solution is one of the main obstacles to reaching lower limits of detection. Using the turn-off detection approach, there are two possible ways to increase the LOD. One is implementing a washing step to remove the excess unbound MNP labels and another is decreasing the number of MNPs in the solution to increase the fraction of bound MNP labels at low RCP concentration. The former is not desirable as it complicates the assay process and is a step away from mix and measure concept in homogeneous assays. On the other hand, increasing the fraction bound by using a low concentration of MNP probes would extend the LOD. The fraction bound is an essential parameter in any biosensor. In MNP based biosensor, the fraction bound is the ratio of the target bound MNPs, N_{bound}, to the total number of MNP probes, N_{total}, in the solution and is proportional to the sensor signal:

$$fb = \frac{N_{bound}}{N_{total}} \propto signal. \tag{4.2}$$

The fraction bound for a NC sample is zero, as there is no target for the MNPs to bind. At very high concentration of the target, where all the MNP probes are bound with the target, the fraction bound reaches 100% and the sensor is fully saturated. In order to detect a particular concentration of the target, the number of MNPs should be chosen in a way that a measurable fraction of the total MNP probes are bound. For instance, Tian et al. has reported 780 fM LOD for RCPs using 5 µg/mL MNP probes in the turn-off detection strategy [118]. This is 15 times better LOD compared to the previous experiments in the same setup using 100 µg/mL of MNP probes [51]. Such an improvement in the LOD is an inherent result of 20 times decrease in the MNP concentration (total number of labels) which has increased the fraction bound at the reported target concentration. This improvement, however, comes at the price of limited dynamic range, and slower binding dynamics of MNP labels with the RCPs, which could result in longer total testing time for the biosensor.

Table 4.1: Performance of magnetic sensor systems using RCA for detection of nucleic acid targets. The 100 nm MNPs reported in this table from different sensors are the same MNP system used in our experiments.

Sensors	**MNP size**	**assay time**	**LOD**	**Linear dynamic range**
LTS SQUID [78]	130 nm	125 min	3.7 pM	2 orders of magnitude
DynoMag [114]	100 nm	100 min	5 pM	2 orders of magnitude
DynoMag [80]	50, 130 and 250 nm	125 min	4 pM	not defined
Optomagnetic [51]	100 nm	93 min	10 pM	2 orders of magnitude
Optomagnetic [118]	100 nm + 250 nm	110 min	780 fM	2 orders of magnitude
Anisotropic magnetoresistance [119]	80 nm	110 min	2 pM	2 orders of magnitude
Electron paramagnetic resonance [120]	100 nm	76 min	1 pM	2 orders of magnitude
HTS SQUID (paper II)	100 nm	110 min	1 pM	2 orders of magnitude
Induction coils (paper V)	100 nm	110 min	1 pM	2 orders of magnitude

The modification of the DynoMag system to include sample tubes and a peristaltic pump system instead of the vials and stepper motors have decreased the distance between the sample and pick-up coils and provided better control over small sample volumes. The results of magnetic ac susceptibility measurement of RCPs in turn-off approach using this method is presented in paper V, and the system shows improved LOD compared to the commercially available DynoMag system. There are, however, possibilities of improving the detection limits and performance of our systems or generally many of these magnetic biosensors which use the same principle of operation. Using more optimal MNP systems with magnetic materials other than iron-oxide that would have a higher magnetic moment to label the RCPs would improve the limit of detection of the systems. For instance, cobalt particles have at least 2 times higher magnetization compared to the MNPs used in our experiments and would give twice higher signals [121]. The assay can also be modified to increase the number of MNPs binding to each RCP by optimizing the salt concentration in the buffer solution for opening the RCP which is a large DNA strand folding on itself. One can also use DNA templates during the RCA in order to impose topological strain on the RCPs and avoid folding of the DNA macromolecules. This would provide access to the binding sites which may not be otherwise reachable inside the RCP folded coil by the MNPs. Magnetic incubation during the hybridization process has been shown to improve the binding kinetics [122] which could also be used to decrease the total assay time.

The sensitivity of the turn-off approach depends strongly on the inaccuracies in the initial concentration of the MNP labels, the precision of measuring the reference signal, and the stability of the MNP system. The first two factors are particularly important because the sensor should resolve a small reduction in an already existing significant signal, especially when measuring low concentrations of the RCPs (target analyte). In this scenario, the SNR is rather small, and one has to reduce the concentration of the MNP labels to reach a more considerable drop in the reference signal. It is also possible to correct the signal levels to the initial concentration of the MNPs by normalizing the measured ac magnetic susceptibility using the high-frequency component of the ac magnetic susceptibility, χ_∞. This high-frequency real part depends only

on the concentration of the MNPs, and for MNP labels of 100 nm in size can be measured at frequencies as low as 10 kHz [80, 116]. As discussed above, the stability of the MNP system is also critical. Signal variations due to the MNP instability in the solution affect the quantification of the RCPs and limits the LOD.

4.2 Turn-on detection of RCPs

An alternative approach to the turn-off detection strategy is to use the differential ac susceptibility measurement technique introduced in the Sec. 3.4.2. In this method, a single ac susceptibility measurement compares the difference in the magnetic content of two samples filling two independent microfluidic channels. When the same magnetic sample fills both channels, the result is a zero-response signal. The amplitude of the zero-response signal is less than 1% of the one from magnetic samples in either of the two channels. As the difference in the concentration of the magnetic content in the two sample increases, a signal appears whose magnitude only increases with increasing difference in the two samples. Therefore, the differential method is a turn-on technique which can be used for detection of the RCPs independent of the initial concentration of the MNP labels.

The principle of the differential ac susceptibility measurement is quite similar to the Wheatstone bridge circuit. This circuit is used to measure an unknown resistor or very small variations in a known resistance, R_x. This is performed by having an adjustable resistor,R_2 resistor, on the left arm of the bridge and a known ratio on the right arm of the bridge (R_3/R_4), Fig. 4.4 (a). In this circuit, when the ratio of the left arm of the bridge (R_x/R_2) is equal to the ratio of the two resistors in the right arm (R_3/R_4), there is zero current flowing between points b and d ($V_{bd} = 0$) and the bridge is balanced. The value of the unknown resistor is then extracted from the three other known resistors:

$$\frac{V_{bd}}{V_{ac}} = \frac{R_x}{R_x + R_2} - \frac{R_4}{R_3 + R_4} = 0$$
$$R_x = \frac{R_2 \times R_3}{R_4}. \tag{4.3}$$

In this scenario, the excitation voltage across points a and c (V_{ac}) can be increased to improve the V_{bd} for sensitive measurement of any change in the resistance of R_x without having a large background voltage drop across b and d. If a known resistor is used instead of an adjustable resistor in R_2, one can use the the voltage drop V_{bd} (or current passing between points a and b) to calculate the resistance of the unknown resistor, R_x. In our differential ac susceptibility measurement setup, the the SQUID measures voltage drop across b and d and the R_2 and R_x resistors are taken as the NC and the test sample, Fig. 4.4 (b). The known ratio on the right arm of the bridge is equal to one as the gradiometer compares the magnetic fluxes in its two loops. The SQUID voltage, in this case, yields the difference between the two samples, which will be zero if the test sample is the same as the NC sample.

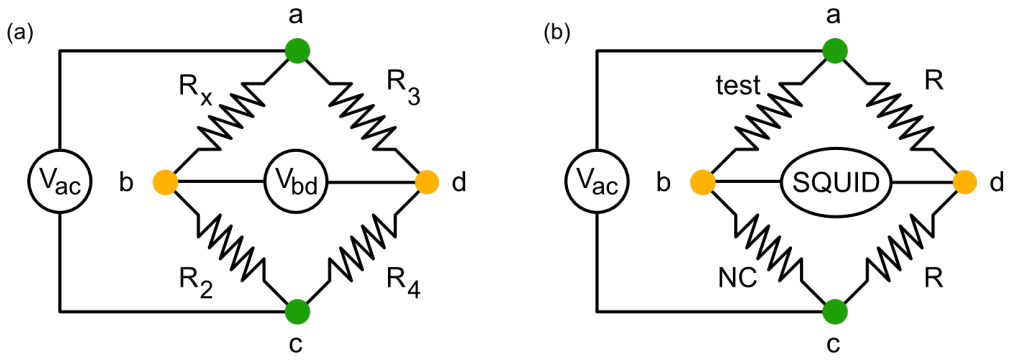

Figure 4.4: (a) A Wheatstone bridge circuit. This circuit is used to either measure an unknown resistor or changes in an known resistro, R_x, using two balanced arms of resistors. The voltage is applied between points a and c and the adjusting resistor R_2 is used to null the voltage drop across points b and d. The unknown resistor can thus be calculated: $R_x = \frac{R_2 \times R_3}{R_4}$. (b) Equivalent circuit of the Wheatstone bridge for the differential ac magnetic susceptibility measurement setup.

Turn-on detection of RCPs is reported earlier in the literature using LTS SQUID magnetometers [87] and optomagnetic sensors [86]. The turn-on detection signals in both of these cases are low-frequency signals

(below 10 Hz) which appear due to the formation of large MNP-RCP complexes. Measurements at low frequencies, however, have some drawbacks. The SNR is lower at lower frequencies, which requires sampling for longer periods. This makes the measurements longer and more complicated. Using the differential ac susceptibility technique for turn-on detection approach opens the whole frequency window for detection because it removes all the magnetic background from the unbound MNP labels. This method also provides more information regarding the binding of the MNPs to the RCP compared to the turn-off approach. The turn-on detection of RCPs using the differential ac susceptibility measurement and further discussions regarding the binding kinetics are presented in papers III and IV.

4.2.1 Principle of turn-on detection

As discussed in the Sec. 3.4.2, the zero detection signal only starts to build up if there are any discrepancies in the concentrations and/or size distributions of the MNP samples in the two channels. Positive test samples containing different concentrations of RCPs of synthetic *V. Cholerae* DNA targets are prepared (amplified for 20 minutes) and measured with NC sample containing the same amount of MNPs (particle concentration of 250 µg/mL or 250 pM). The consumption of the MNPs in the positive test sample due to the formation of MNP-RCP complex results in a small difference in the MNPs' concentration and size distribution in the two samples. The formation of these complexes results in a non-zero-response signal in the differential ac susceptibility measurement, which increases with increasing RCP concentration in the positive test sample.

Fig. 4.5 (a) shows the turn-on detection of RCPs in the imaginary part of differential ac susceptibility for an increasing concentrations of RCPs from 0 to 90.4 pM. Assuming that the magnetic moment of individual MNP does not depend on its volume, the amplitude of the imaginary component of the ac susceptibility is proportional to the concentration of the MNPs. The increase of the peak amplitude in the imaginary component is only due to the change of the MNP size distribution in the positive test sample. The MNPs in the positive test sample bind to the RCPs, which increases their hydrodynamic size, and their characteristic

relaxation moves to lower frequencies. The turn-on detection signal at the Brownian relaxation frequency of the unbound MNPs (at 64.5 Hz) is a function of the RCP concentration. The equilibrium fraction bound is, therefore,

$$fb_{eq} \propto \frac{\chi''_{RCP}}{\chi''_{max}}, \tag{4.4}$$

where the χ''_{max} is the saturation signal (signal amplitude form the NC sample in Ch. 1) and the χ''_{RCP} is the signal levels from different concentrations of RCPs, c.f. Fig. 4.5 (a). The RCP concentration dependence of the fraction bound follows a logistic function behavior [123, 124] and is shown in Fig. 4.5 (b). The experimental LOD is 45 fM with three orders of magnitude working dynamic range. The saturation of the turn-on signal at 90.4 pM concentration of RCPs is due to nearly complete consumption of the MNP labels by the RCPs (100% fraction bound). Increasing the initial concentration of MNP labels would extend the saturation level and the dynamic range of the biosensor. Although the equilibrium fraction bound is not so high at the lower concentrations of RCPs, the effective fraction bound measured by the SQUID sensor is high (is equal to 50%) at low concentrations. This is due to the fact that the differential measurement removes the signals from all the unbound MNPs from the positive test sample in Ch. 2. The detection signal thus comes only from the MNP-RCP complexes in positive test sample (Ch. 2) and the difference of unbound MNPs in the two channels. It is thus analogous to a washing step, where the excess number of unbound labels is removed from the positive test sample, and results in an effective binding fraction of 50%.

4.2.2 MNP-RCP complex relaxation dynamics

The MNP-RCP ensemble has two relaxation frequencies corresponding to particles of two different sizes: (I) a high relaxation frequency (HRF) which is characteristic of the unbound MNPs and (II) a low relaxation frequency (LRF) which is a result of the MNP-RCP complexes or agglomerates. Fitting a bi-modal Cole-Cole model to the data presented in Fig. 4.5 (a) shows that the turn-on detection signal has two distinct

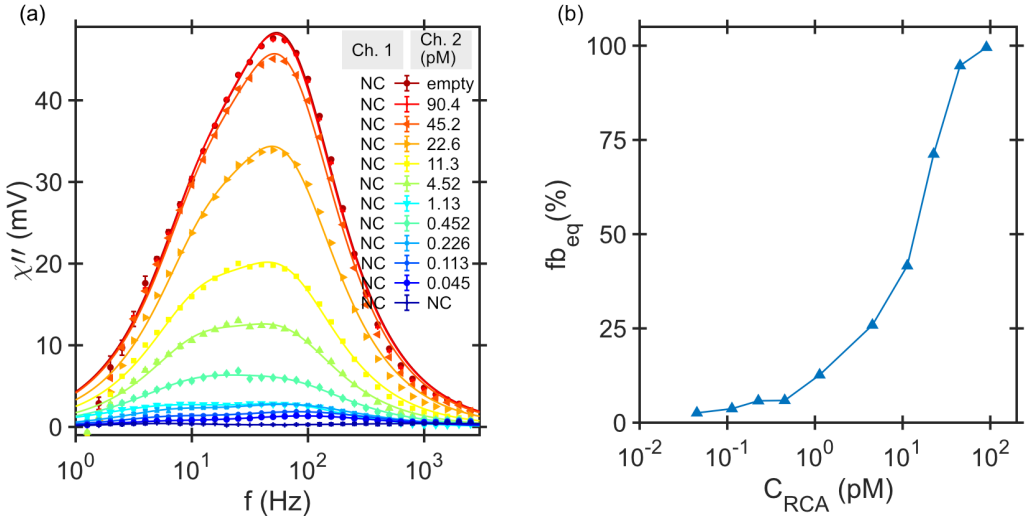

Figure 4.5: Turn-on detection of RCPs using differential ac susceptibility measurements. (a) Imaginary components of differential ac susceptibility versus the frequency for positive test samples containing different concentrations of RCPs ranging from 0 to 90.4 pM in a 3.6 µL sample volume. The NC sample fills Ch. 1, and the positive test samples fill Ch. 2. The solid lines are bi-modal Cole-Cole model fitted to the data points at each RCP concentration. (b) Equilibrium fraction bound is the normalized imaginary signal of the ac susceptibility at 64.5 Hz versus the concentration of the DNA targets (RCPs). The LOD is 45 fM, and the working range spans more than 3 orders of magnitude in target concentration. Adapted from paper III.

relaxation frequencies indeed. The LRF peak corresponds to the Brownian relaxation of the MNP-RCP complex in the positive test sample and the HRF peak is due to unbound MNPs and its magnitude corresponds to the relative difference between unbound MNPs in the test and the NC samples. Fig. 4.6 shows the frequencies of these two peaks extracted by fitting the imaginary part of the differential ac susceptibility using a bi-modal Brownian relaxation model as a function of RCP concentration in the positive test sample.

The extracted frequencies from the bi-modal distribution in the turn-on detection (the LRF and the HRF) implies that the smaller particles in the MNP size distribution are more likely to take precedence in binding during the hybridization with the RCPs. As the RCP concentration increases, the values of both the LRF and the HRF reaches those of the NC sample. This shows that the formation of the agglomerates at higher concentrations of the RCPs takes the LRF distribution out of the measurement window. If the LRF peak is taken as the turn-on

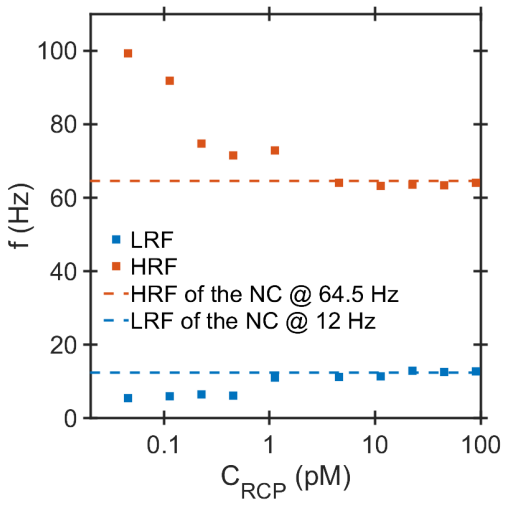

Figure 4.6: The extracted LRF and HRF frequencies versus the RCP concentration in the positive test sample. For high concentration of RCPs, both the LRF and HRF are shifted to 12 and 64.5 Hz, respectively. These two frequencies corresponds to the LRF and HRF of the intrinsic bi-modal distribution of the NC sample. Adapted from paper IV.

detection signal, it is therefore important to remember that this signal disappears at higher RCP concentrations due to agglomeration of the MNPs and RCPs. The effect of RCP concentration and formation of the agglomerates in the turn-on detection approach signal are discussed in the paper IV.

We have also reported and discussed the effect of RCA time and RCP concentration in both turn-on and turn-off approaches (paper IV). The turn-on approach advantage over turn-off detection scheme is not limited only to the LOD of target analyte (RCPs or target DNA molecules). The turn-on approach can clearly distinguish the LRF and HRF peaks corresponding to the MNP-RCP complexes and the unbound MNP even at very low concentrations of RCPs. It also provides crucial information regarding the binding process of the MNP to RCPs that can be used to optimize the biosensor.

CHAPTER 5

Conclusion

A nucleic acid magnetic biosensor based on a high-T_c SQUID gradiometer sensor has been demonstrated to have an excellent experimental limit of detection (45 fM at SNR = 100), and fast turn-around time (60 min). The DNA assay implements RCA for volume amplification of the DNA target molecule into a long DNA coil or the rolling circle product (RCP). The magnetic ac susceptibility measurement was used to detect the specific binding of the MNPs to the RCPs. An advantage of using the ac susceptibility is low background signal. The detection signal is the imaginary component of the ac susceptibility which is unique to the MNP response.

The differential ac magnetic susceptibility technique developed in this work, paper III, has overcome one of the challenges of turn-off detection approaches in homogeneous magnetic biosensors: the magnetic background from the unbound MNPs. The method is a magnetic analogous of the Wheatstone bridge which allows measurement of small differences in two MNP solutions. The simultaneous measurement of the NC and the test sample reduces the overall turn-around time of the assay. This method also provides more information regarding the binding of the MNPs to the RCPs even at low concentrations of the target which is not

available in turn-off detection approaches (paper IV). The measurement technique is a paradigm shift in homogeneous magnetic biosensors.

One of the drawbacks of our sensor, however, is the need for liquid nitrogen to operate our high-T_c SQUID. As presented in paper I, we have shown successful operation of the high-T_c SQUID with great noise performance utilizing a commercial two-stage micro electro mechanical systems (MEMS) based Joule-Thomson micro-cooler (DEMCON Kryoz). The micro-cooler offers long operation time, simple usage, and temperature stability and adjustment. With proper magnetic shielding, the SQUID sensor can be operated stably over a long time in the micro-cooler using only nitrogen gas bottles.

The sensitivity of our differential magnetic bioassay is determined by the quality of the MNP system rather than the magnetic sensitivity of our SQUID sensor. This means that one could use other magnetic sensors with lower sensitivity compare to SQUIDs to reach the same limits of detection. The induction coil system presented in Paper V is an excellent example. It already uses a first order gradiometer but only to remove the contributions of the applied excitation field. Implementing the differential ac susceptibility measurement technique on this system would boost its sensitivity by increasing the SNR levels.

Further work is required for the high-T_c SQUID biosensor to be implemented for practical field applications. In the sensor part, this includes using a closed cycle dry cooler to rule out the need for liquid or gas nitrogen completely. On the other hand, the nucleic acid assay should be fully implemented on a lab-on-a-chip to automate the diagnostic test and eliminate any need of trained staffs or clinical labs.

APPENDIX A

RCA protocol

A.1 Ligation and RCA

Throughout this work, synthetic DNA targets of *Vibrio Cholerae* is used. The DNA sequences for the synthetic target and their corresponding padlock probe and detection oligonucleotide which are necessary to perform RCA are presented in Table A.1. The procedure which has been used to produce final RCPs of 5 nM concentration is explained in the following sections. The 5 nM concentration corresponds to the initial concentration of the padlock probes. Considering the 22.6% success rate of the amplification process [95], the final concentration is 1.13 nM.

In order to form a padlock probe-target complex, 3 µL synthesized target DNA (1 µM) is hybridized and ligated at 37 °C for 15 min with 1 µL padlock probe (1 µM) in a solution consisting of 2.5 µL of 20 mM adenosine triphosphate (ATP), 1 µL T4 DNA ligase (1U/µL, enzyme unit per micro liter), and 5 µL of Φ29 DNA polymerase buffer in a total volume of 50 µL. The circularized padlock probe-target complex is now ready for amplification. To amplify the padlock probes, 25 µL ligation mix consisting of 20 nM concentration of padlock probes are copied by 0.4 µL Φ29 polymerase for 1 hour at 37 °C in a solution with

4 µL dNTP (2.5 mM), 6 µL bovine serum albumin (BSA) (2 µg/mL), 6 µL Φ29 polymerase buffer and water in 60 µL reaction volume. The enzyme is thermally inactivated at 65°C for 5 min. 40 µL hybridization buffer of 1 M tris(hydroxymethyl) aminomethane hydrochloride (Tris-HCl) (pH 8.0), 0.5 M ethylenediaminetetraacetic acid (EDTA), Tween-20 (10%) and 5 M sodium chloride (NaCl) is added at the end to bring the concentration of RCPs to 5 nM [80]. The RCP solution is now ready to be labelled for detection.

Table A.1: DNA sequences for the synthetic *V. Cholerae* target used in this thesis and its corresponding padlock probe and the detection oligonucleotide.

Oligos	**Sequences from 5′ to 3′**
Target	CCC TGG GCT CAA CCT AGG AAT CGC ATT TG
Padlock probe	TAG GTT GAG CCC AGG GAC TTC TAG AGT GTA CCG ACC TCA GTA GCC GTG ACT ATC GAC TTG TTG ATG TCA TGT GTC GCA CCA AAT GCG ATT CC
Detection probe	TTT TTT TTT TTT TTT TTT TTG TTG ATG TCA TGT GTC GCAC

A.2 Functionalization of MNPs

The coupling of the oligonucleotides to the MNPs is performed in a volume of 100 µL. The MNPs are washed twice using a magnetic separator in a washing buffer with 1 M Tris-HCl (pH 8.0), 0.5 M EDTA, Tween-20 (10%) and 5 M NaCl. The MNPs are then resuspended in 50 µL washing buffer. 6 µL of the oligonucleotide with 10 µM concentration is added to the resuspended MNPs, and the mixture is vortexed and incubated at room temperature for 30 min. After the incubation the MNPs are rewashed in the washing buffer for two times using a permanent magnet and resuspended to the original volume of 100 µL in PBS with a pH of 7.4. With the oligonucleotides bound to the surface, the MNPs are functionalized and can specifically bind to the backbone of the padlock probe amplified by the RCA method (i.e., RCPs). The MNP systems used in our studies, according to its datasheet, are suspended iron oxide-based streptavidin-coated multi-core particles with a median diameter of 80 or 100 nm for the core (micromod Partikeltechnologie GmbH, Rostock, Germany).

A.3 Labelling of RCPs

In this study, we have labeled the RCPs with the fluorescent markers (atto-488) or MNPs. The atto-488 are attached to the $3'$ side of the detection probe oligonucleotide and have their excitation wavelength in the range of the laser wavelength used in the NTA setup. The detection probe oligonucleotides also have a biotinylated side in its $5'$ which can bind to the streptavidin coating of the MNPs, functionalizing them for specific binding to the RCPs. In order to conjugate the fluorescent or the magnetic markers to the RCPs, the markers and the RCPs are mixed, and the solution is incubated for 20-30 min at 55 °C. Different concentrations of RCPs are prepared by diluting the RCP stock solution with hybridization buffer.

Bibliography

[1] *Pandemic Influenza Risk Management WHO Interim Guidance*. Tech. rep. World Health Organization, 2013.

[2] C. Viboud and L. Simonsen. "Global mortality of 2009 pandemic influenza A H1N1". *The Lancet Infectious Diseases* 12.9 (2012), pp. 651–653. DOI: 10.1016/S1473-3099(12)70152-4.

[3] B. Jester, T. Uyeki, and D. Jernigan. "Readiness for Responding to a Severe Pandemic 100 Years After 1918". *American Journal of Epidemiology* 187.12 (2018), pp. 2596–2602. DOI: 10.1093/aje/kwy165.

[4] C. D. Kelly-Cirino et al. "Importance of diagnostics in epidemic and pandemic preparedness". *BMJ Global Health* 4.Suppl 2 (2019), e001179. DOI: 10.1136/bmjgh-2018-001179.

[5] M. L. Wilson, K. A. Fleming, M. A. Kuti, L. M. Looi, N. Lago, and K. Ru. "Access to pathology and laboratory medicine services: a crucial gap". *The Lancet* 391.10133 (2018), pp. 1927–1938. DOI: 10.1016/S0140-6736(18)30458-6.

[6] F. J. Gruhl, B. E. Rapp, and K. Länge. "Biosensors for Diagnostic Applications". In: Springer, Berlin, Heidelberg, 2011, pp. 115–148. DOI: 10.1007/10_2011_130.

[7] D. G. Buerk. *Biosensors : theory and applications*. Technomic Pub. Co, 1993, p. 221.

[8] M. A. Morales and J. M. Halpern. "Guide to Selecting a Biorecognition Element for Biosensors". *Bioconjugate Chemistry* 29.10 (2018), pp. 3231–3239. DOI: 10.1021/acs.bioconjchem.8b00592.

[9] C. Karunakaran, R. Rajkumar, and K. Bhargava. "Introduction to Biosensors". *Biosensors and Bioelectronics* (2015), pp. 1–68. DOI: 10.1016/B978-0-12-803100-1.00001-3.

[10] S. Chen and M. H. Shamsi. "Biosensors-on-chip: a topical review". *Journal of Micromechanics and Microengineering* 27 (2017), p. 083001. DOI: 10.1088/1361-6439/aa7117.

[11] J. Kirsch, C. Siltanen, Q. Zhou, A. Revzin, and A. Simonian. "Biosensor technology: recent advances in threat agent detection and medicine". *Chemical Society Reviews* 42.22 (2013), pp. 8733–8768. DOI: 10.1039/c3cs60141b.

[12] I. A. Darwish. "Immunoassay Methods and their Applications in Pharmaceutical Analysis: Basic Methodology and Recent Advances." *International journal of biomedical science* 2.3 (2006), pp. 217–235. DOI: 10.1016/S0166-526X(03)40010-X.

[13] Y. Du and S. Dong. "Nucleic acid biosensors: Recent advances and perspectives". *Analytical Chemistry* 89.1 (2017), pp. 189–215. DOI: 10.1021/acs.analchem.6b04190.

[14] D. K. Yang, J. L. Huang, C. C. Chen, H. J. Su, and J. C. Wu. "Enhancement of target-DNA hybridization efficiency by pre-hybridization on sequence-orientated micro-arrayed probes". *Journal of the Chinese Institute of Chemical Engineers* 39.3 (2008), pp. 187–193. DOI: 10.1016/j.jcice.2007.12.012.

[15] "The polymerase chain reaction". *Advances in Physiology Education* 28.2 (2004). Ed. by K. B. Mullis, F. Ferre, and R. A. Gibbs, pp. 44–50. DOI: 10.1152/advan.00002.2004.

[16] T. Notomi, H. Okayama, H. Masubuchi, T. Yonekawa, K. Watanabe, N. Amino, and T. Hase. "Loop-mediated isothermal amplification of DNA". *Nucleic acids research* 28.12 (2000), E63. DOI: 10.1093/nar/28.12.e63.

[17] M. Wiedmann, W. I. Wilson, J. Luo, F. Barany, and A. Batt. "Ligase Chain Reaction Applications". *Genome Research* 3: (1994), S51–S64.

[18] J. Banér, M. Nilsson, M. Mendel-Hartvig, and U. Landegren. "Signal amplification of padlock probes by rolling circle replication". *Nucleic Acids Research* 26.22 (1998), pp. 5073–5078. DOI: 10.1093/nar/26.22.5073.

[19] C. Jianrong, M. Yuqing, H. Nongyue, W. Xiaohua, and L. Sijiao. "Nanotechnology and biosensors". *Biotechnology Advances* 22.7 (2004), pp. 505–518. DOI: 10.1016/J.BIOTECHADV.2004.03.004.

[20] P. Sarihi, A. Azadkhah Shalmani, V. Araban, and M. Raoufi. "Nanoparticles for Biosensing". In: Springer, Cham, 2019, pp. 121–143. DOI: 10.1007/978-3-030-10834-2_5.

[21] Y.-T. Chen et al. "Biosensing Using Magnetic Particle Detection Techniques". *Sensors* 17.10 (2017), pp. 2300–2336. DOI: 10.3390/s17102300.

[22] P. D'Orazio. "Biosensors in clinical chemistry — 2011 update". *Clinica Chimica Acta* 412.19-20 (2011), pp. 1749–1761. DOI: 10.1016/J.CCA.2011.06.025.

[23] Q. A. Pankhurst, J. Connolly, S. K. Jones, and J. Dobson. "Applications of magnetic nanoparticles in biomedicine". *Journal of Physics D: Applied Physics* 36.13 (2003), R167–R181. DOI: 10.1088/0022-3727/36/13/201.

[24] S. Schrittwieser et al. "Homogeneous biosensing based on magnetic particle labels". *Sensors (Switzerland)* 16.6 (2016). DOI: 10.3390/s16060828.

[25] J. Kudr, Y. Haddad, L. Richtera, Z. Heger, M. Cernak, V. Adam, and O. Zitka. "Magnetic Nanoparticles: From Design and Synthesis to Real World Applications". *Nanomaterials* 7.9 (2017), p. 243. DOI: 10.3390/nano7090243.

[26] A. H. Lu, E. L. Salabas, and F. Schüth. "Magnetic nanoparticles: Synthesis, protection, functionalization, and application". *Angewandte Chemie - International Edition* 46.8 (2007), pp. 1222–1244. DOI: 10.1002/anie.200602866.

[27] A. Sandhu. "Biosensing: New probes offer much faster results". *Nature Nanotechnology* 2.12 (2007), pp. 746–748. DOI: 10.1038/nnano.2007.398.

[28] C. I. Justino, T. A. Rocha-Santos, A. C. Duarte, and T. A. Rocha-Santos. "Review of analytical figures of merit of sensors and biosensors in clinical applications". *TrAC Trends in Analytical Chemistry* 29.10 (2010), pp. 1172–1183. DOI: 10.1016/J.TRAC.2010.07.008.

[29] H. C. Tekin and M. A. Gijs. "Ultrasensitive protein detection: A case for microfluidic magnetic bead-based assays". *Lab on a Chip* 13.24 (2013), pp. 4711–4739. DOI: 10.1039/c3lc50477h.

[30] T. A. Rocha-Santos. "Sensors and biosensors based on magnetic nanoparticles". *TrAC - Trends in Analytical Chemistry* 62 (2014), pp. 28–36. DOI: 10.1016/j.trac.2014.06.016.

[31] D. Issadore et al. "Magnetic sensing technology for molecular analyses". *Lab on a Chip* 14.14 (2014), pp. 2385–2397. DOI: 10.1039/c4lc00314d.

[32] R. S. Gaster et al. "Quantification of protein interactions and solution transport using high-density GMR sensor arrays". *Nature Nanotechnology* 6.5 (2011), pp. 314–320. DOI: 10.1038/nnano.2011.45.

[33] J. B. Haun, T.-J. Yoon, H. Lee, and R. Weissleder. "Magnetic nanoparticle biosensors". *Wiley Interdisciplinary Reviews: Nanomedicine and Nanobiotechnology* 2.3 (2010), pp. 291–304. DOI: 10.1002/wnan.84.

[34] A. P. Astalan, F. Ahrentorp, C. Johansson, K. Larsson, and A. Krozer. "Biomolecular reactions studied using changes in Brownian rotation dynamics of magnetic particles". *Biosensors and Bioelectronics* 19.8 (2004), pp. 945–951. DOI: 10.1016/j.bios.2003.09.005.

[35] K. Enpuku, Y. Tsujita, K. Nakamura, T. Sasayama, and T. Yoshida. "Biosensing utilizing magnetic markers and superconducting quantum interference devices". *Superconductor Science and Technology* 30.5 (2017). DOI: 10.1088/1361-6668/aa5fce.

[36] M. Nilsson, H. Malmgren, M. Samiotaki, M. Kwiatkowski, B. P. Chowdhary, and U. Landegren. "Padlock probes: Circularizing oligonucleotides for localized DNA detection". *Science* 265.5181 (1994), pp. 2085–2088. DOI: 10.1126/science.7522346.

[37] Q. A. Pankhurst, N. T. K. Thanh, S. K. Jones, and J. Dobson. "Progress in applications of magnetic nanoparticles in biomedicine". *Journal of Physics D: Applied Physics* 42.22 (2009), p. 224001. DOI: 10.1088/0022-3727/42/22/224001.

[38] K. M. Krishnan. "Biomedical Nanomagnetics: A Spin Through Possibilities in Imaging, Diagnostics, and Therapy". *IEEE Transactions on Magnetics* 46.7 (2010), pp. 2523–2558. DOI: 10.1109/TMAG.2010.2046907.

[39] A. V. Bychkova, O. N. Sorokina, M. A. Rosenfeld, and A. L. Kovarski. "Multifunctional biocompatible coatings on magnetic nanoparticles". *Russian Chemical Reviews* 81.11 (2012), pp. 1026–1050. DOI: 10.1070/RC2012v081n11ABEH004280.

[40] G. Liu, J. Gao, H. Ai, and X. Chen. "Applications and Potential Toxicity of Magnetic Iron Oxide Nanoparticles". *Small* 9.9-10 (2013), pp. 1533–1545. DOI: 10.1002/smll.201201531.

[41] A. P. Khandhar, R. M. Ferguson, and K. M. Krishnan. "Monodispersed magnetite nanoparticles optimized for magnetic fluid hyperthermia: Implications

in biological systems". *Journal of Applied Physics* 109.7 (2011), 07B310. DOI: 10.1063/1.3556948.

[42] S. Chikazumi. *Physics of Ferromagnetism*. OXFORD UNIVERSITY PRESS, 1997.

[43] C. P. Bean and J. D. Livingston. "Superparamagnetism". *Journal of Applied Physics* 30.4 (1959), S120–S129. DOI: 10.1063/1.2185850.

[44] A. H. Morrish. *The physical principle of magnetism*. New York: The Institute of Electrical and Electronics Engineers, Inc., 2001. DOI: 10.1002/9780470546581.

[45] A. Cayless, S. Hoon, B. Tanner, R. Chantrell, and M. Kilner. "High sensitivity measurements of Néel relaxation in fine particle ferromagnetic systems". *Journal of Magnetism and Magnetic Materials* 30.3 (1983), pp. 303–311. DOI: 10.1016/0304-8853(83)90068-9.

[46] S. Bogren et al. "Classification of Magnetic Nanoparticle Systems—Synthesis, Standardization and Analysis Methods in the NanoMag Project". *International Journal of Molecular Sciences* 16.9 (2015), pp. 20308–20325. DOI: 10.3390/ijms160920308.

[47] J. Wells et al. "Standardisation of magnetic nanoparticles in Liquid Suspension". *Journal of Physics D: Applied Physics* 50.38 (2017), p. 383003. DOI: 10.1088/1361-6463/aa7fa5.

[48] F. Ahrentorp et al. "Effective particle magnetic moment of multi-core particles". *Journal of Magnetism and Magnetic Materials* 380 (2015), pp. 221–226. DOI: 10.1016/j.jmmm.2014.09.070.

[49] C. B. Kriz, K. Rådevik, and D. Kriz. "Magnetic Permeability Measurements in Bioanalysis and Biosensors" (1996). DOI: 10.1021/AC951227T.

[50] I. Koh and L. Josephson. "Magnetic Nanoparticle Sensors". *Sensors* 9.10 (2009), pp. 8130–8145. DOI: 10.3390/s91008130.

[51] M. Donolato et al. "Novel readout method for molecular diagnostic assays based on optical measurements of magnetic nanobead dynamics". *Analytical Chemistry* 87.3 (2015), pp. 1622–1629. DOI: 10.1021/ac503191v.

[52] L. Lartigue et al. "Nanomagnetic Sensing of Blood Plasma Protein Interactions with Iron Oxide Nanoparticles: Impact on Macrophage Uptake". *ACS Nano* 6.3 (2012), pp. 2665–2678. DOI: 10.1021/nn300060u.

[53] P.-A. Besse, G. Boero, M. Demierre, V. Pott, and R. Popovic. "Detection of a single magnetic microbead using a miniaturized silicon Hall sensor". *Applied Physics Letters* 80.22 (2002), pp. 4199–4201. DOI: 10.1063/1.1483909.

[54] G. Mihajlović, P. Xiong, S. von Molnár, K. Ohtani, H. Ohno, M. Field, and G. J. Sullivan. "Detection of single magnetic bead for biological applications using an InAs quantum-well micro-Hall sensor". *Applied Physics Letters* 87.11 (2005), p. 112502. DOI: 10.1063/1.2043238.

[55] K. Togawa, H. Sanbonsugi, A. Sandhu, M. Abe, H. Narimatsu, K. Nishio, and H. Handa. "High sensitivity InSb hall effect biosensor platform for DNA detection and biomolecular recognition using functionalized magnetic nanobeads". *Japanese Journal of Applied Physics, Part 2: Letters* 44.46-49 (2005). DOI: 10.1143/JJAP.44.L1494.

[56] D. R. Baselt, G. U. Lee, M. Natesan, S. W. Metzger, P. E. Sheehan, and R. J. Colton. "A biosensor based on magnetoresistance technology". *Biosensors and Bioelectronics* 13.7-8 (1998), pp. 731–739. DOI: 10.1016/S0956-5663(98)00037-2.

[57] S. Wang and Guanxiong Li. "Advances in Giant Magnetoresistance Biosensors With Magnetic Nanoparticle Tags: Review and Outlook". *IEEE Transactions on Magnetics* 44.7 (2008), pp. 1687–1702. DOI: 10.1109/TMAG.2008.920962.

[58] R. S. Gaster, D. A. Hall, and S. X. Wang. "NanoLAB: An ultraportable, handheld diagnostic laboratory for global health". *Lab on a Chip* 11.5 (2011), pp. 950–956. DOI: 10.1039/c0lc00534g.

[59] A. Prieto Astalan, C. Jonasson, K. Petersson, J. Blomgren, D. Ilver, A. Krozer, and C. Johansson. "Magnetic response of thermally blocked magnetic nanoparticles in a pulsed magnetic field". *Journal of Magnetism and Magnetic Materials* 311.1 SPEC. ISS. (2007), pp. 166–170. DOI: 10.1016/j.jmmm.2006.10.1182.

[60] R. Kötitz, W. Weitschies, L. Trahms, W. Brewer, and W. Semmler. "Determination of the binding reaction between avidin and biotin by relaxation measurements of magnetic nanoparticles". *Journal of Magnetism and Magnetic Materials* 194.1-3 (1999), pp. 62–68. DOI: 10.1016/S0304-8853(98)00580-0.

[61] D. Eberbeck, C. Bergemann, S. Hartwig, U. Steinhoff, and L. Trahms. "Binding kinetics of magnetic nanoparticles on latex beads studied by magnetorelaxometry". *Applied Organometallic Chemistry* 18.10 (2004), pp. 542–547. DOI: 10.1002/aoc.758.

[62] F. Öisjöen, J. F. Schneiderman, A. P. Astalan, A. Kalabukhov, C. Johansson, and D. Winkler. "A new approach for bioassays based on frequency- and time-domain measurements of magnetic nanoparticles". *Biosensors and Bioelectronics* 25.5 (2010), pp. 1008–1013. DOI: 10.1016/j.bios.2009.09.013.

[63] C. P. Moerland, L. J. van IJzendoorn, and M. W. J. Prins. "Rotating magnetic particles for lab-on-chip applications – a comprehensive review". *Lab on a Chip* 19.6 (2019), pp. 919–933. DOI: 10.1039/C8LC01323C.

[64] J. Dieckhoff, M. Schilling, and F. Ludwig. "Fluxgate based detection of magnetic nanoparticle dynamics in a rotating magnetic field". *Applied Physics Letters* 99.11 (2011), p. 112501. DOI: 10.1063/1.3639276.

[65] J. H. Dieckhoff, T. Yoshida, K. Enpuku, M. Schilling, and F. Ludwig. "Homogeneous bioassays based on the manipulation of magnetic nanoparticles by rotating and alternating magnetic FieldsA comparison". *IEEE Transactions on Magnetics* 48.11 (2012), pp. 3792–3795. DOI: 10.1109/TMAG.2012.2198797.

[66] J. Connolly and T. G. St Pierre. "Proposed biosensors based on time-dependent properties of magnetic fluids". *Journal of Magnetism and Magnetic Materials* 225.1-2 (2001), pp. 156–160. DOI: 10.1016/S0304-8853(00)01245-2.

[67] P. J. W. Debye. *Polar Molecules*. New Yor: Chemical Catalog Co., Inc., 1929, p. 174.

[68] P. C. Fannin, S. W. Charles, and T. Relihan. "On the influence of inertial effects, arising from rotational Brownian motion, on the complex susceptibility of ferrofluids". *Journal of Physics D: Applied Physics* 28.9 (1995), pp. 1765–1769. DOI: 10.1088/0022-3727/28/9/002.

[69] M. Hanson. "The frequency dependence of the complex susceptibility of magnetic liquids". *Journal of Magnetism and Magnetic Materials* 96.1-3 (1991), pp. 105–113. DOI: 10.1016/0304-8853(91)90617-J.

[70] C. V. Topping and S. J. Blundell. "A.C. susceptibility as a probe of low-frequency magnetic dynamics". *Journal of Physics: Condensed Matter* 31.1 (2019), p. 013001. DOI: 10.1088/1361-648X/aaed96.

[71] V. L. Calero-Ddelc, D. I. Santiago-Quiñonez, and C. Rinaldi. "Quantitative nanoscale viscosity measurements using magnetic nanoparticles and SQUID AC susceptibility measurements". *Soft Matter* 7.9 (2011), pp. 4497–4503. DOI: 10.1039/c0sm00902d.

[72] P. C. Fannin, B. K. Scaife, and S. W. Charles. "The measurement of the frequency dependent susceptibility of magnetic colloids". *Journal of Magnetism and Magnetic Materials* 72.1 (1988), pp. 95–108. DOI: 10.1016/0304-8853(88)90276-4.

[73] F. Ludwig, C. Balceris, C. Jonasson, and C. Johansson. "Analysis of AC Susceptibility Spectra for the Characterization of Magnetic Nanoparticles". *IEEE Transactions on Magnetics* 53.11 (2017), pp. 0–3. DOI: 10.1109/TMAG.2017.2693420.

[74] K. S. Cole and R. H. Cole. "Dispersion and absorption in dielectrics I. Alternating current characteristics". *The Journal of Chemical Physics* 9.4 (1941), pp. 341–351. DOI: 10.1063/1.1750906.

[75] S. H. Chung, A. Hoffmann, S. D. Bader, C. Liu, B. Kay, L. Makowski, and L. Chen. "Biological sensors based on Brownian relaxation of magnetic nanoparticles". *Applied Physics Letters* 85.14 (2004), pp. 2971–2973. DOI: 10.1063/1.1801687.

[76] S. H. Chung et al. "Biological sensing with magnetic nanoparticles using Brownian relaxation (invited)". *Journal of Applied Physics* 97.10 (2005). DOI: 10.1063/1.1853694.

[77] A. Fornara et al. "Tailored magnetic nanoparticles for direct and sensitive detection of biomolecules in biological samples". *Nano Letters* 8.10 (2008), pp. 3423–3428. DOI: 10.1021/nl8022498.

[78] M. Strömberg, J. Göransson, K. Gunnarsson, M. Nilsson, P. Svedlindh, and M. Strømme. "Sensitive Molecular Diagnostics Using Volume-Amplified Magnetic Nanobeads". *Nano Letters* 8.3 (2008), pp. 816–821. DOI: 10.1021/nl072760e.

[79] M. F. Hansen, M. Donolato, J. Fock, M. Strömberg, M. Strømme, and P. Svedlindh. "Sensor Systems with Magnetic and Optomagnetic Readout of Rolling Circle Amplification Products". In: *Rolling Circle Amplification (RCA)*. Ed. by V. V. Demidov. Cham: Springer International Publishing, 2016. Chap. 11, pp. 123–138. DOI: 10.1007/978-3-319-42226-8_11.

[80] T. Zardán Gómez De La Torre, A. Mezger, D. Herthnek, C. Johansson, P. Svedlindh, M. Nilsson, and M. Strømme. "Detection of rolling circle amplified DNA molecules using probe-tagged magnetic nanobeads in a portable AC susceptometer". *Biosensors and Bioelectronics* 29.1 (2011), pp. 195–199. DOI: 10.1016/j.bios.2011.08.019.

[81] C. Y. Hong, C. C. Wu, Y. C. Chiu, S. Y. Yang, H. E. Horng, and H. C. Yang. "Magnetic susceptibility reduction method for magnetically labeled immunoassay". *Applied Physics Letters* 88.21 (2006), pp. 2004–2007. DOI: 10.1063/1.2206557.

[82] C. Y. Hong, W. S. Chen, Z. F. Jian, S. Y. Yang, H. E. Horng, L. C. Yang, and H. C. Yang. "Wash-free immunomagnetic detection for serum through magnetic susceptibility reduction". *Applied Physics Letters* 90.7 (2007), pp. 88–91. DOI: 10.1063/1.2536127.

[83] J. J. Chieh, S. Y. Yang, Z. F. Jian, W. C. Wang, H. E. Horng, H. C. Yang, and C. Y. Hong. "Hyper-high-sensitivity wash-free magnetoreduction assay on biomolecules using high- Tc superconducting quantum interference devices". *Journal of Applied Physics* 103.1 (2008). DOI: 10.1063/1.2827359.

[84] P. I. Nikitin, P. M. Vetoshko, and T. I. Ksenevich. "New type of biosensor based on magnetic nanoparticle detection". *Journal of Magnetism and Magnetic Materials* 311.1 SPEC. ISS. (2007), pp. 445–449. DOI: 10.1016/j.jmmm.2006.10.1180.

[85] S. H. Liao et al. "Time-dependent phase lag of biofunctionalized magnetic nanoparticles conjugated with biotargets studied with alternating current magnetic susceptometor for liquid phase immunoassays". *Applied Physics Letters* 103.24 (2013). DOI: 10.1063/1.4846536.

[86] R. S. Bejhed, T. Zardán Gómez de la Torre, M. Donolato, M. F. Hansen, P. Svedlindh, and M. Strömberg. "Turn-on optomagnetic bacterial DNA sequence detection using volume-amplified magnetic nanobeads". *Biosensors and Bioelectronics* 66 (2015), pp. 405–411. DOI: 10.1016/j.bios.2014.11.048.

[87] M. Strömberg, T. Zardán Gómez de la Torre, J. Göransson, K. Gunnarsson, M. Nilsson, M. Strømme, and P. Svedlindh. "Microscopic mechanisms influencing the volume amplified magnetic nanobead detection assay". *Biosensors and Bioelectronics* 24.4 (2008), pp. 696–703. DOI: 10.1016/j.bios.2008.06.043.

[88] Y. Zhao, F. Chen, Q. Li, L. Wang, and C. Fan. "Isothermal Amplification of Nucleic Acids". *Chemical Reviews* 115.22 (2015), pp. 12491–12545. DOI: 10.1021/acs.chemrev.5b00428.

[89] V. Gubala, L. F. Harris, A. J. Ricco, M. X. Tan, and D. E. Williams. "Point of care diagnostics: Status and future". *Analytical Chemistry* 84.2 (2012), pp. 487–515. DOI: 10.1021/ac2030199.

[90] M. Fakruddin, K. B. Mannan, M. Hossain, S. Islam, R. Mazumdar, A. Chowdhury, and M. Chowdhury. "Nucleic acid amplification: Alternative methods of polymerase chain reaction". *Journal of Pharmacy and Bioallied Sciences* 5.4 (2013), p. 245. DOI: 10.4103/0975-7406.120066.

[91] D.-O. Antson, A. Isaksson, U. Landegren, and M. Nilsson. "PCR-generated padlock probes detect single nucleotide variation in genomic DNA". *Nucleic Acids Research* 28.12 (2000), 58e–58. DOI: 10.1093/nar/28.12.e58.

[92] T. Zardán Gómez de la Torre. "Detection of Biomolecules using volume-amplified magnetic nanobeads". PhD thesis. Uppsala University, 2012.

[93] R. Jansson. "Development of a solid-phase padlock probe technology using microfluidics". MA thesis. Uppsala University, 2007.

[94] N. Dekoning. "A Rolling Circle Amplification-Based Methodology for Making Long , Sequence- Repeating , DNA Duplexes". MA thesis. Chalmers University of Technology, 2018.

[95] M. Kühnemund, I. Hernández-Neuta, M. I. Sharif, M. Cornaglia, M. A. Gijs, and M. Nilsson. "Sensitive and inexpensive digital DNA analysis by microfluidic enrichment of rolling circle amplified single-molecules". *Nucleic Acids Research* 45.8 (2017). DOI: 10.1093/nar/gkw1324.

[96] H. Kuhn, V. V. Demidov, and M. D. Frank-Kamenetskii. "Rolling-circle amplification under topological constraints". *Nucleic Acids Research* 30.2 (2002), pp. 574–580. DOI: 10.1093/nar/30.2.574.

[97] L. Mahmoudian, N. Kaji, M. Tokeshi, M. Nilsson, and Y. Baba. "Rolling circle amplification and circle-to-circle amplification of a specific gene integrated with electrophoretic analysis on a single chip". *Analytical Chemistry* 80.7 (2008), pp. 2483–2490. DOI: 10.1021/ac702289j.

[98] B. Schweitzer et al. "Immunoassays with rolling circle DNA amplification: A versatile platform for ultrasensitive antigen detection". *Proceedings of the National Academy of Sciences* 97.18 (2000), pp. 10113–10119. DOI: 10.1073/pnas.170237197.

[99] W. Zhao, Y. Gao, S. A. Kandadai, M. A. Brook, and Y. Li. "DNA polymerization on gold nanoparticles through rolling circle amplification: Towards novel scaffolds for three-dimensional periodic nanoassemblies". *Angewandte Chemie - International Edition* 45.15 (2006), pp. 2409–2413. DOI: 10.1002/anie.200600061.

[100] W. Cheng, F. Yan, L. Ding, H. Ju, and Y. Yin. "Cascade signal amplification strategy for subattomolar protein detection by rolling circle amplification and quantum dots tagging". *Analytical Chemistry* 82.8 (2010), pp. 3337–3342. DOI: 10.1021/ac100144g.

[101] B. Carr and M. Wright. "Nanoparticle Tracking Analysis: a review of applications and usage 2012-2012". *NanoSight Ltd* 1.0 (2012), p. 188.

[102] D. Koelle, R. Kleiner, F. Ludwig, E. Dantsker, and J. Clarke. "High-transition-temperature superconducting quantum interference devices". *Reviews of Modern Physics* 71.3 (1999), pp. 631–686. DOI: 10.1103/RevModPhys.71.631.

[103] F. Öisjöen, P. Magnelind, A. Kalabukhov, and D. Winkler. "High-Tc SQUID gradiometer system for immunoassays". *Superconductor Science and Technology* 21.3 (2008). DOI: 10.1088/0953-2048/21/3/034004.

[104] J. Clarke and A. I. B. Eds. *The SQUID Handbook*. Vol. I. Weinheim, FRG: Wiley, 2004. DOI: 10.1002/3527603646.

[105] S. Ruffieux et al. "The role of kinetic inductance on the performance of YBCO SQUID magnetometers" (2019).

[106] P. P. P. M. Lerou et al. "Fabrication of a micro cryogenic cold stage using MEMS-technology". *Journal of Micromechanics and Microengineering* 16.10 (2006), pp. 1919–1925. DOI: 10.1088/0960-1317/16/10/002.

[107] H. Becker and C. Gärtner. "Polymer microfabrication technologies for microfluidic systems". *Analytical and Bioanalytical Chemistry* 390.1 (2008), pp. 89–111. DOI: 10.1007/s00216-007-1692-2.

[108] A. Dietzel. *Microsystems for Pharmatechnology*. Ed. by A. Dietzel. Cham: Springer International Publishing, 2016. DOI: 10.1007/978-3-319-26920-7.

[109] J. C. Mcdonald, D. C. Duffy, J. R. Anderson, and D. T. Chiu. "Review General Fabrication of microfluidic systems in poly (dimethylsiloxane)". *Electrophoresis* 21 (2000), pp. 27–40.

[110] S. Sepehri. *Ultra-sensitive measurements of magnetically labelled RCA products in a microfluidic channel using a high-Tc SQUID*. Licentiate thesis. Chalmers University of Technology. 2018.

[111] J. Dieckhoff, D. Eberbeck, M. Schilling, and F. Ludwig. "Magnetic-field dependence of Brownian and Néel relaxation times". *Journal of Applied Physics* 119.4 (2016). DOI: 10.1063/1.4940724.

[112] D. Kim and A. E. Herr. "Protein immobilization techniques for microfluidic assays". *Biomicrofluidics* 7.4 (2013), p. 041501. DOI: 10.1063/1.4816934.

[113] H. Zhang and M. Chiao. "Anti-fouling coatings of poly(dimethylsiloxane) devices for biological and biomedical applications". *Journal of Medical and Biological Engineering* 35.2 (2015), pp. 143–155. DOI: 10.1007/s40846-015-0029-4.

[114] F. Ahrentorp et al. "Sensitive magnetic biodetection using magnetic multi-core nanoparticles and RCA coils". *Journal of Magnetism and Magnetic Materials* 427.September 2016 (2017), pp. 14–18. DOI: 10.1016/j.jmmm.2016.10.041.

[115] S. Akhtar et al. "Real-space transmission electron microscopy investigations of attachment of functionalized magnetic nanoparticles to DNA-coils acting as a biosensor". *Journal of Physical Chemistry B* 114.41 (2010), pp. 13255–13262. DOI: 10.1021/jp105756b.

[116] M. Strömberg, T. Zardán Gómez de la Torre, M. Nilsson, P. Svedlindh, and M. Strømme. "A magnetic nanobead-based bioassay provides sensitive detection of single- and biplex bacterial DNA using a portable AC susceptometer". *Biotechnology Journal* 9.1 (2014), pp. 137–145. DOI: 10.1002/biot.201300348.

[117] M. Donolato et al. "Quantification of rolling circle amplified DNA using magnetic nanobeads and a Blu-ray optical pick-up unit". *Biosensors and Bioelectronics* 67 (2015), pp. 649–655. DOI: 10.1016/j.bios.2014.09.097.

[118] B. Tian, T. Zardán Gómez De La Torre, M. Donolato, M. F. Hansen, P. Svedlindh, and M. Strömberg. "Multi-scale magnetic nanoparticle based optomagnetic bioassay for sensitive DNA and bacteria detection". *Analytical Methods* 8.25 (2016), pp. 5009–5016. DOI: 10.1039/c6ay00721j.

[119] R. S. Bejhed et al. "On-chip detection of rolling circle amplified DNA molecules from Bacillus globigii spores and Vibrio cholerae". *Small* 10.14 (2014), pp. 2877–2882. DOI: 10.1002/smll.201303325.

[120] B. Tian, X. Liao, P. Svedlindh, M. Strömberg, and E. Wetterskog. "Ferromagnetic Resonance Biosensor for Homogeneous and Volumetric Detection of DNA". *ACS Sensors* 3 (2018), pp. 1093–1101. DOI: 10.1021/acssensors.8b00048.

[121] R. N. Grass, E. K. Athanassiou, and W. J. Stark. "Covalently Functionalized Cobalt Nanoparticles as a Platform for Magnetic Separations in Organic Synthesis". *Angewandte Chemie International Edition* 46.26 (2007), pp. 4909–4912. DOI: 10.1002/anie.200700613.

[122] A. Mezger et al. “Scalable DNA-Based Magnetic Nanoparticle Agglutination Assay for Bacterial Detection in Patient Samples”. *ACS Nano* 9.7 (2015), pp. 7374–7382. DOI: 10.1021/acsnano.5b02379.

[123] J. Dieckhoff, S. Schrittwieser, J. Schotter, H. Remmer, M. Schilling, and F. Ludwig. “Single-core magnetic markers in rotating magnetic field based homogeneous bioassays and the law of mass action”. *Journal of Magnetism and Magnetic Materials* 380 (2015), pp. 205–208. DOI: 10.1016/j.jmmm.2014.10.088.

[124] C. C. Yang, S. Y. Yang, J. J. Chieh, H. E. Horng, C. Y. Hong, and H. C. Yang. “Universal behavior of biomolecule-concentration-dependent reduction in ac magnetic susceptibility of bioreagents”. *IEEE Magnetics Letters* 3 (2012), p. 1500104. DOI: 10.1109/LMAG.2012.2183858.